Supplementary Information for

'Poly(ions-water ligand) network' electrolyte enables high-voltage high-conductivity aqueous metal-ions chemistries

Tianfeng Qin,[1] Hao Chen[1], Wenzhang Fang,[1] Guozhong Cao[2] and Chao Gao[1]*

[1] MOE Key Laboratory of Macromolecular Synthesis and Functionalization, Department of Polymer Science and Engineering, International Research Center for X Polymers, Key Laboratory of Adsorption and Separation Materials and Technologies of Zhejiang Province, Zhejiang University, Hangzhou 310027, China.

[2] Department of Materials Science and Engineering University of Washington Seattle, WA 98195-2120, USA.

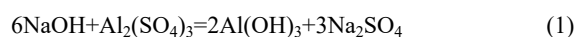* E-mail:chaogao@zju.edu.cn.

Part 1. Experimental part

Materials: $Al_2(SO_4)_3 \cdot 18H_2O$ (AR, 99%), $ZnSO_4 \cdot H_2O$ (AR, 99%), $CsOH \cdot H_2O$ (AR, 99%), $KAl(SO_4)_2 \cdot 12H_2O$ (AR, 99.5%) and $NH_3 \cdot H_2O$ (25 wt% ~ 28 wt%) are bought from Shanghai Aladdin Bio-Chem Technology Co., Ltd, China. Na_2SO_4 (AR, 99%), K_2SO_4 (AR, 99%), KOH (AR, 99%), and NaOH (AR, 99%) are purchased from Sinopharm Chemical Reagent Co., LTD, China. Cs_2SO_4 (AR, 99%) is bought from Hangzhou Bangyi Chemical Co., LTD. Graphene oxide (GO) with average lateral size of 10 μm was acquired from GaoxiTech Co., LTD, China. The GO is washed with deionized water for six times. The density of GO aqueous solution is 0.8 g mL^{-1}. The density of GO sheets is 3.78 mg mL^{-1}. Carbon cloth (CC, model number LS-CF-220, thickness 264 mm) is purchased from Shanghai Lishuo Composite Materials Co. LTD, China. All reagents were used as received without any further treatment. Deionized water is generated by PW Ultrapure Water System and has a resistivity of 18 $M\Omega$ cm^{-1}.

For the preparation of quasi-solid-state electrolyte containing the transparent crystal sheets, 12.9 g Na_2SO_4, and 8.16 g $Al_2(SO_4)_3 \cdot 18H_2O$ are added gradually to a beaker containing 38.56 g deionized water to form a clear solution by the magnetic stirring, in which the beaker is placed simultaneously in oil bath at 80 °C. After stirring for 1 h, the beaker containing saturated $NaAl(SO_4)_2 \cdot 12H_2O$ solution is placed in the lab at about 10 °C for 24 h to form transparent crystal sheets. The characterizations on the quasi-solid-state electrolyte of transparent crystal sheets are shown in Figure S1.
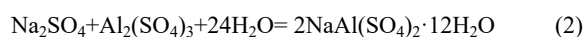
For the preparation of SAH, 14.402 g $Al_2(SO_4)_3 \cdot 18H_2O$ (0.36 M) is added to a (glass) beaker containing 60 mL deionized water to form a transparent solution by the magnetic stirring at 35 °C. After adding 4 g NaOH (1.6 M) sheets into the above transparent solution, (1) the solution color transforms into white; (2) the white solution becomes solid state rapidly, which can be stirred using a glass rod to make it become a fluid; (3) the temperature of white solution increases to 48.8 °C due to the exothermic reaction of NaOH sheets dissolved into water, which needs to be cooled by putting the beaker containing the white solution in the water bath containing the deionized water for 5 minutes; (4) the water vapor adhered to the inner wall of beaker is observed. The beaker containing white solution is placed in the lab at 25 °C after stirring for 5 minutes and becomes "solid-state" after 24 hours. After 15 days, the sodium alum hydrogel (SAH) can be used to carry out the characterizations.

For the preparation of 'poly(ions-water ligand) network' electrolyte (PINE), the beaker containing 60 mL 1 M Na_2SO_4 (8.608 g) aqueous solution is used to continue the same procedures as SAH. The white solution become two parts composed of the liquid supernatant and the solid-state gel at the bottom of beaker after placing 24 hours in the lab at 25 °C. After 15 days, the liquid supernatant is poured into the tank containing wasted liquids. The solid-state hydrogel is denoted as 'poly(ions-water ligand) network' electrolyte (PINE) and used to carry out the characterizations on FTIR, Raman, and so on.

The synthesis process of sol-gel is based on the following formulas:

$$6NaOH+Al_2(SO_4)_3=2Al(OH)_3+3Na_2SO_4 \qquad (1)$$

1.6mol/L   0.36mol/L(excess)

$$Na_2SO_4+Al_2(SO_4)_3+24H_2O= 2NaAl(SO_4)_2 \cdot 12H_2O \qquad (2)$$

0.1mol/L   0.1mol/L(0.006 mol from (1))

In which, the volume of deionized water is 60 mL based on the volume without adding agents.

Based on the amount of Na_2SO_4 and $Al_2(SO_4)_3 \cdot 18H_2O$ used to prepare the quasi-solid-state electrolyte containing the transparent crystal sheets, the concentration of $Al_2(SO_4)_3 \cdot 18H_2O$ is increased to 0.36 mol L^{-1} (14.402 g, excess), and NaOH 1.6 mol L^{-1} (4 g,). For the reaction formula (1), $Al(OH)_3$ sol can be formed, the amount of $Al_2(SO_4)_3$ is excess to make the reaction formula (2) possible. The temperature of 48.8 °C derived from the exothermic reaction

of NaOH sheets dissolving into water could guarantee the formation of the amorphous $NaAl(SO_4)_2 \cdot 12H_2O$ sol. It is well known that the particles of $Al(OH)_3$ sol are positively charged. The SAH composed of amorphous $Al(OH)_3$ sol and amorphous $NaAl(SO_4)_2 \cdot 12H_2O$ sol can be stable without the coagulation at 25 °C may due to the repulsive force of positive charge. It can be inferred that the particles of amorphous $NaAl(SO_4)_2 \cdot 12H_2O$ sol could be positively charged, or else the coagulation occurs. The addition of Na_2SO_4 as the coagulation agent leads to the coagulation of amorphous $NaAl(SO_4)_2 \cdot 12H_2O$ sol and the formation of gel.

For the preparation of Al(OH)₃ gel, based on the formula of $NaOH + Al_2(SO_4)_3 = Al(OH)_3 + Na_2SO_4$, 10.641 g $Al_2(SO_4)_3 \cdot 18H_2O$ (0.266 mol) is added into a beaker containing 60 mL deionized water to form a homogeneous solution by the magnetic stirring at 35 °C. Then, 4 g NaOH (1.6 mol L^{-1}) is added successively. The clear solution becomes white solid state rapidly, which can be stirred using a glass rod to make it become a fluid. Finally, the beaker is placed in lab at 25 °C for 24 h.

For the preparation of Al(OH)₃ gel with the addition of 1 mol L⁻¹ Na₂SO₄, all the procedures are the same as the preparation of $Al(OH)_3$, except from the addition of 8.608 g Na_2SO_4 into deionized water. The coagulation does not happen.

For the preparation of control hydrogel using NH₃·H₂O, the method is the same as PINE. The differences are (1) that replacing NaOH sheets with 13.45 mL $NH_3 \cdot H_2O$ (25 wt%) to form 1.6 M aqueous solution, and (2) that decreasing the volume of deionized water decreases to 46.55 mL.

For the preparation of PINE with the different concentrations of Na₂SO₄ (e.g., 0.5 M, 1 M, 2 M, and 3 M) is prepared as the control samples, and denoted as PINE-0.5 M, PINE-1 M (that is PINE), PINE-2 M, and PINE-3 M, respectively. The white solution become two parts composed of the liquid supernatant and the solid-state gel at the bottom of beaker after placing 15 days in the lab at 25 °C. The liquid supernatant is poured in the tank containing wasted liquid. The solid-state hydrogel is used to carry out the characterizations on FTIR, Raman, and so on.

For the preparation of PASSH (potassium alum solid-state hydrogel), the method is the same as PINE, just replacing Na_2SO_4 and NaOH with K_2SO_4 and KOH, respectively. 14.402 g $Al_2(SO_4)_3 \cdot 18H_2O$ (0.36 M) is added to a beaker containing 60 mL 1 M K_2SO_4 (10.561 g, 1 M) aqueous solution to form a transparent solution by the magnetic stirring. After adding KOH (5.441 g, 1.6 M) into the above transparent solution, the solution color transforms into white. The beaker is placed in the lab at 25 °C. After 15 days, the white solution become two parts composed of the liquid supernatant and the solid-state gel at the bottom of beaker. The liquid supernatant is poured out after about 3 days. The potassium alum solid-state hydrogel (PASSH) at the bottom of beaker can be used to carry out the characterizations.

For the preparation of CASSH (caesium alum solid-state hydrogel), the method is the same as PINE, just replacing Na_2SO_4 and NaOH with Cs_2SO_4 and CsOH, respectively. 14.402 g $Al_2(SO_4)_3 \cdot 18H_2O$ (0.36 M) is added to a beaker containing 60 mL 1 M Cs_2SO_4 (21.733 g, 1 M) aqueous solution to form a transparent solution by the magnetic stirring. After adding $CsOH \cdot H_2O$ (16.969 g, 1.6 M) into the above transparent solution, the solution color transforms into white. The beaker is placed in the lab at 25 °C. After 15 days, the white solution become two parts composed of the liquid supernatant and the solid-state gel at the bottom of beaker. The liquid supernatant is poured out after 3 days. The caesium alum solid-state hydrogel (CASSH) at the bottom of beaker can be used to carry out the characterizations.

For the preparation of re-crystallization PASSH, a re-crystallization method at room temperature is used. 1 M K_2SO_4 and 0.72 M $KAl(SO_4)_2 \cdot 12H_2O$ are added into a beaker with 60 mL deionized water. The solution is stirred and heated at 70 °C for 1 h in a water bath due to the low solubility of $KAl(SO_4)_2 \cdot 12H_2O$. The beaker is placed in lab at 25 °C. The precipitated crystal from the supersaturated solution is observed at the bottom of beaker after one day.

For the preparation of re-crystallization PASSH-KOH, the method is similar to re-crystallization PASSH.

After completely dissolved into solution of 1 M K_2SO_4 and 0.72 M $KAl(SO_4)_2 \cdot 12H_2O$, 5.44 g KOH is added and dissolved into the above solution. The beaker is placed in lab at 25 °C for 15 days. The white re-crystallization PASSH-KOH is observed at the bottom of beaker.

For the preparation of PASSH', PASSH'-KOH1, PASSH'-KOH2, PASSH'-KOH3, the method is similar to re-crystallization PASSH with some differences. The mass of K_2SO_4 and $KAl(SO_4)_2 \cdot 12H_2O$ is 38.2 g and 4.8 g, respectively, with the ratio of about 8:1. The mass of deionized water is 57 g. The temperature and time of water bath are 80 °C and 45 min, respectively. KOH with different mass is added into the precursor solution. PASSH' represents the mass of KOH is 0 g. PASSH'-KOH1 represents the mass of KOH is 0.644 g. PASSH'-KOH2 represents the mass of KOH is 1.4 g. PASSH'-KOH3 represents the mass of KOH is 2.8 g.

For the preparation of NZSSSH, using the method of preparing SAH, 1 M $ZnSO_4 \cdot H_2O$ (10.768 g) is added into the cooled precursor of SAH under stirring for 5 minutes. The white solution become two parts composed of the white liquid and the solid-state hydrogel at the bottom of beaker after placing 15 days in the lab at 25 °C. The liquid is poured in the tank containing wasted liquid. The solid-state hydrogel denoted as NZSSSH is used to carry out the characterizations on FTIR, Raman, and so on.

For the preparation of NZSSSH and GO, using the method of preparing NZSSSH, 10.5 mL GO aqueous solution containing 39.69 mg GO nanosheets is added into the precursor of NZSSSH. The solid-state hydrogel denoted as NZSSSH and GO, is utilized to carry out the characterizations after placing 15 days in the lab at 25 °C.

For the preparation of NZSSSH and GO with the different GO content (NZSSSH and 0.20 wt‰ GO, NZSSSH and 0.40 wt‰ GO, NZSSSH and 0.65 wt‰ GO, and NZSSSH and 0.90 wt‰ GO), the method is the same as the NZSSSH, but some parameters are changed. The total volume of NZSSSH and GO is fixed at 70.5 mL. For NZSSSH and 0.2 wt‰ GO, the deionized water and GO aqueous solution are 65.5 and 5 mL, respectively. The mass ratio of GO sheets to the total mass is ~0.2 wt‰. For NZSSSH and 0.40 wt‰ GO, the deionized water and GO aqueous solution are 60 and 10.5 mL, respectively. The mass ratio of GO sheets to the total mass is ~0.40 wt‰. For NZSSSH and 0.65 wt‰ GO, the deionized water and GO aqueous solution are 54 and 16.50 mL, respectively. The mass ratio of GO sheets to the total mass is ~0.65 wt‰. For NZSSSH and 0.90 wt‰ GO, the deionized water and GO aqueous solution are 47.20 and 23.30 mL, respectively. The mass ratio of GO sheets to the total mass is ~0.90 wt‰.

Preparation of OCC as negative electrode, CC is treated by CV technique in the three-electrode configuration. The electrolyte is a saturated K_2SO_4 aqueous solution. CC (1×1 cm^2), Pt plate (2×2 cm^2), and saturated calomel electrode, are employed as the working electrode, the counter electrode, and the reference electrode, respectively. The scan rate of 25 mV s^{-1} and 100 cycles are selected to start the CV process together with the subsequent scan rate of 100 mV s^{-1} and 300 cycles. The obtained CC is denoted as OCC and directly used as electrode in the following experiments.

The fabrication of visual in-situ OCC//CC based on the different hydrogels, OCC (negative electrode) and CC (positive electrode) are immersed into the precursors of hydrogels to form the visual in-situ energy storage devices, and cycled in the voltage window of 0~2.1 V at a current density for 500 cycles before the other electrochemical characterizations.

Characterizations

X-ray diffraction (XRD, X' Pert3 Powder-17005730, Cu-Kα irradiation, 0.154056 nm) is used to confirm the phase of samples. Fourier transform infrared (FTIR) spectra are obtained by a Nicolet iS50 spectrometer equipped with an attenuated total reflectance accessory. Nuclear magnetic resonance (NMR) spectra are collected by a Brulcer 600 MHz NMR spectrometer (DMX-600). Raman spectra are recorded by inVia-Reflex (Renishaw plc)

with a laser of 532 nm wavelength. The morphologies of samples are obtained from on a Hitachi S4800 field emission scanning electron microscope (SEM) system. Rheological characterizations of samples are carried out using a rotational rheometer (HAAKE RS6000). Optical microscope is utilized to observe the phase separation of hydrogels. Thermo Gravimetric Analysis (TGA) is carried out using a TA Instruments SDT Q600 V8.2 Build 100. X-ray photoelectron spectroscopy (XPS) is obtained using an ESCALAB 250 photoelectron spectroscopy (Thermo Fisher Scienctific). Element content in PINE and PASSH is detected by inductively coupled plasma photometric emission spectroscopy (ICP-OES, Thermo ICAP PRO).

Electrochemical properties

CV and GCD curves of the energy storage unit are collected on an electrochemical station (CHI 660E). Electrochemical impedance spectroscopy (EIS) measurements are carried out at the open circuit potential with frequencies of 100 kHz to 10 MHz at an amplitude of 5 mV. The long-term cycle was carried out using a Landian battery test system (CT3001A). The capacities are obtained from the GCD curves according to the formula $C= I\Delta t/S$, where I is the constant discharge current density, Δt the discharge time, S the area of the electrode and C the areal capacity. The mass of CC (1×1 cm^2) or OCC (1×1 cm^2) is 18.5 mg. The power density is obtained on the formula of $P = E\times 3600/\Delta t$. The mass energy density was calculated according to the formula of $E = CV^2/2$.

Simulating computation

All calculations were performed using the plane wave based periodic DFT method as implemented in the Vienna Ab Initio Simulation Package (VASP).[1, 2] The electron-ion interaction was described with the projector augmented wave (PAW) method.[3, 4] The electron exchange and correlation energies were treated within the generalized gradient approximation in the Perdew-Burke-Ernzerhof functional (GGA-PBE).[5] The plane wave basis was set up to 500 eV. Computations were satisfied until the energy and force converged within 10^{-6} eV and 0.01 eV A$^{\circ-1}$, respectively.

Adsorption energy is defined as $E_{ad}=E_{total}-E_{H2O}-E_{sub}$, in which E_{ad} is the total energy of the adsorption state of H_2O on the active site, E_{H2O} is the total energy of H_2O and E_{sub} is the total energy of substrate.

The NaAl(SO$_4$)$_2$·12H$_2$O|Na$^+$+SO$_4^{2-}$+12H$_2$O|NaAl(SO$_4$)$_2$·12H$_2$O heterojunction model was set up with NaAl(SO$_4$)$_2$·12H$_2$O (001) surface including 328 atoms in the supercell model of $1\times1\times2$. Ab initio molecular dynamics (AIMD) was carried out to obtain NaAl(SO$_4$)$_2$·12H$_2$O|Na$^+$+SO$_4^{2-}$+12H$_2$O|NaAl(SO$_4$)$_2$·12H$_2$O amorphous configurations.[6] AIMD task was performed over 90000 steps in the NVT ensembles at 600 K using a small-time step of 0.1 fs due to the lightweight of H$^+$.
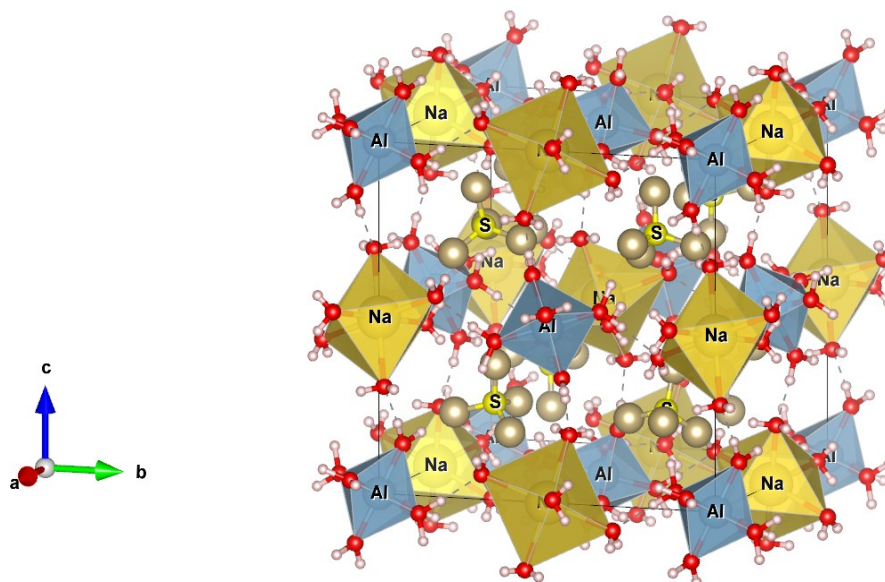
Part 2. Figures and captions

Figure S1 The crystal structure of $NaAl(SO_4)_2 \cdot 12H_2O$. The red ball represents the oxygen, and the pink ball the hydrogen. The earthy yellow ball (oxygen) connects with the sulfur to form SO_4^{2-}. A sodium ion coordinates with 6 water molecules to form $Na(H_2O)_6^+$ octahedron, "Na^+-H_2O ligand". An aluminium ion coordinates with 6 water molecules to form $Al(H_2O)_6^{3+}$ octahedron, "Al^{3+}-H_2O ligand". "Na^+-H_2O ligand" and "Al^{3+}-H_2O ligand" together with SO_4^{2-} form inorganic polymer ($NaAl(SO_4)_2 \cdot 12H_2O$) by hydrogen bond.
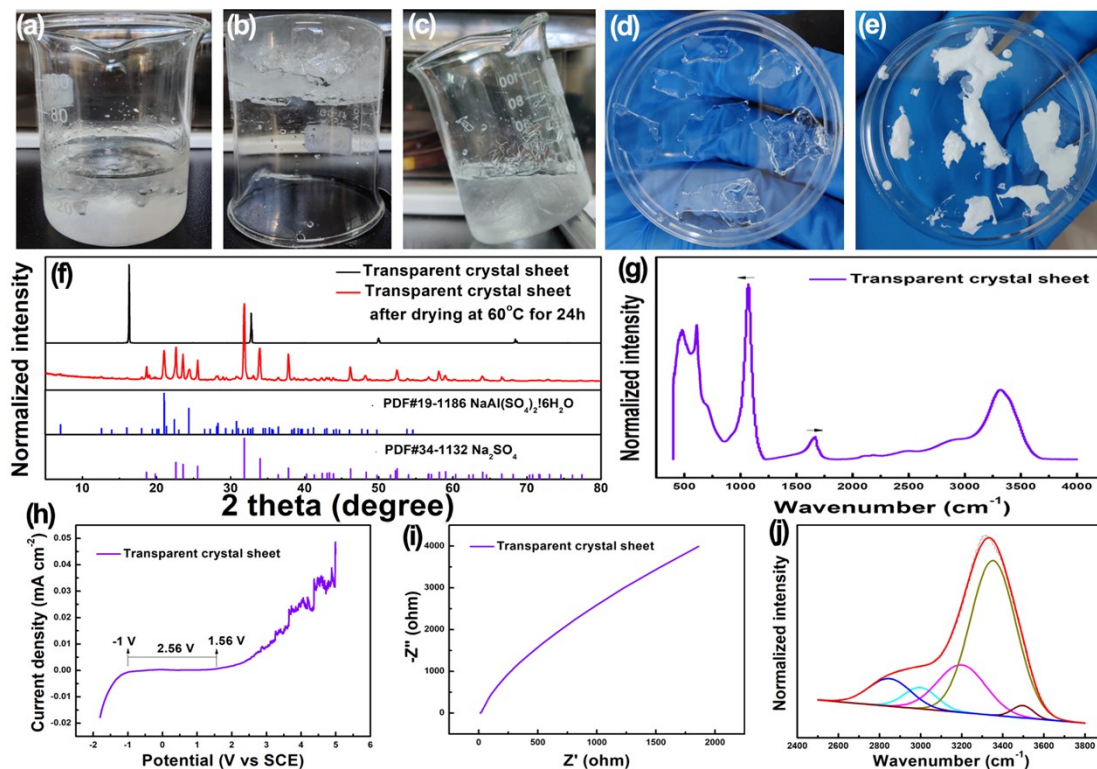
Figure S2 The optical images for (a-c) the quasi-solid-state electrolyte containing transparent crystal sheets. The optical images for (d) the seven transparent crystal sheets on petri dish and (e) the seven transparent crystal sheets on petri dish after drying at 60 °C for 24 h. (f) XRD pattern of the transparent crystal sheet and the transparent crystal sheet after drying at 60 °C for 24 h. (g) and (j) ATR-FTIR spectrum of the transparent crystal sheet. (h) LSV and (i) Nyquist plots for the quasi-solid-state electrolyte.

The quasi-solid-state electrolyte containing the transparent crystal sheets presents a solid-state behavior as shown in Figures S2 (a) and (b). After stirring with the glass rod, it becomes a fluid in Figure S2(c), indicating a fake solid-state behavior. Compared to the transparent crystal sheets in Figure S2(d), after drying at 60 °C for 24 h, it turns into the white crystal sheets as displayed in Figure S2(e) due to the evaporation of ~55 wt% water molecules. XRD patterns are collected to obtain the phase composition. As shown in Figure S2(f), XRD pattern (black) of the transparent crystal sheets presents four sharp diffraction peaks, indicating a high degree of crystallinity. Unfortunately, no PDF card is indexed to match with the pattern. After evaporating water at 60 °C for 24 h, new diffraction peaks are observed in the XRD pattern (red), and indexed to $NaAl(SO_4)_2 \cdot 6H_2O$ (PDF#19-1186) and Na_2SO_4 (PDF#34-1132). It can be inferred that the transparent crystal sheet is composed of $NaAl(SO_4)_2 \cdot 12H_2O$, Na_2SO_4 and H_2O in a certain form. For example, $NaAl(SO_4)_2 \cdot 12H_2O$ microcrystalline is connected with the hydrated ions (Na^+, SO_4^{2-}) by the hydrogen bond. ATR-FTIR spectrum is recorded to demonstrate the hypothesis. As shown in Figure S2(g), the wavenumbers at ~1104 cm^{-1} and 1642 cm^{-1} belong to the v_3 antisymmetric stretching mode (SO_4^{2-}) and the O-H bending in water, respectively. [7, 8] The wavenumbers ranging from ~2500 cm^{-1} to ~3800 cm^{-1} are related to the different hydrogen-bonded O-H in water that is obtained by the peak differentiating analysis as shown in Figure S2(j), in which the wavenumbers at ~3200 cm^{-1}, ~3353 cm^{-1}, ~3498 cm^{-1} are attributed to the strongly hydrogen-bonded O-H, the weakly hydrogen-bonded O-H, and the nearly non-hydrogen-bonded O-H, respectively.[9] The ratio is ~24%, 74%, and 2%, respectively, indicating the predominance of the weakly hydrogen-bonded O-H for water in the transparent crystal sheets. This is consistent with the hypothesis. But the crystal structure of the transparent crystal sheet is still unknown, (e.g., the atoms arrangement).

The quasi-solid-state electrolyte containing the transparent crystal sheets shows a narrow ESW of ~2.56 V in Figure S2(h), and a moderate ionic conductivity of ~29 mS cm^{-1} at 25 °C as shown in Figure S2(i) and Table S1. The narrow ESW is due to the low concentrated Na_2SO_4 aqueous electrolyte between sheets.
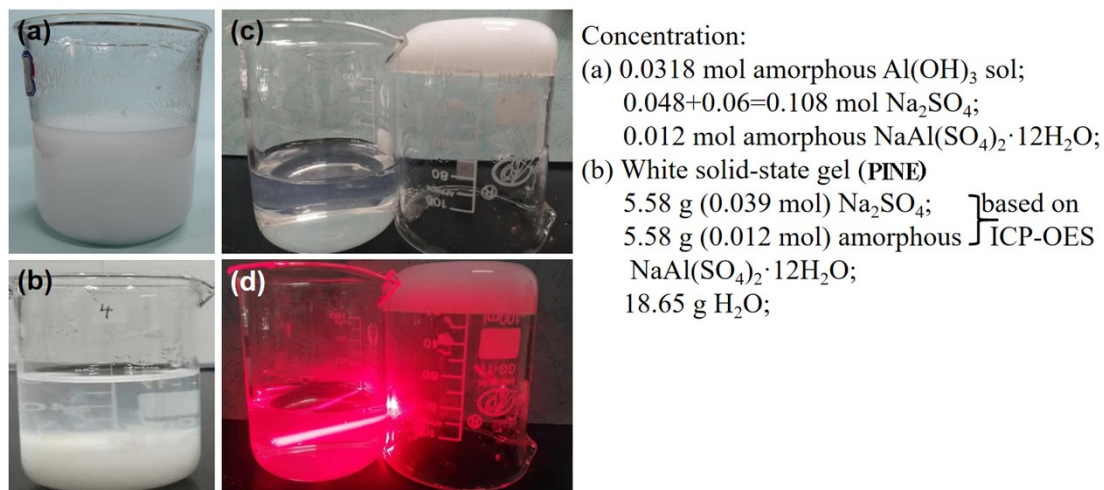

Concentration:
(a) 0.0318 mol amorphous $Al(OH)_3$ sol;
    0.048+0.06=0.108 mol Na_2SO_4;
    0.012 mol amorphous $NaAl(SO_4)_2 \cdot 12H_2O$;
(b) White solid-state gel (**PINE**)
    5.58 g (0.039 mol) Na_2SO_4;   ⎤based on
    5.58 g (0.012 mol) amorphous ⎦ICP-OES
      $NaAl(SO_4)_2 \cdot 12H_2O$;
    18.65 g H_2O;

Figure S3 Sol-gel process. Optical photographs of (a) sol and (b) coagulation and gel. (c) The liquid supernatant and PINE, and (d) Tyndall effect. The liquid supernatant containing $Al(OH)_3$ shows obvious Tydall effect. The results of ICP-OES is in Table S4.

Figure S3(a) is the as-prepared sol consisting of 0.0318 mol amorphous $Al(OH)_3$ sol, 0.108 mol Na_2SO_4 and 0.012 mol amorphous $NaAl(SO_4)_2 \cdot 12H_2O$. By adding coagulation agent of Na_2SO_4, white solid-state gel (PINE) is formed at the bottom of beaker after 15 days. The liquid supernatant in Figure S3(d) shows an obvious Tydall effect after illuminating with the red laser radiation compared to the one without illuminating, in Figure S3(c), demonstrating the existence of colloid $Al(OH)_3$ in the liquid supernatant.
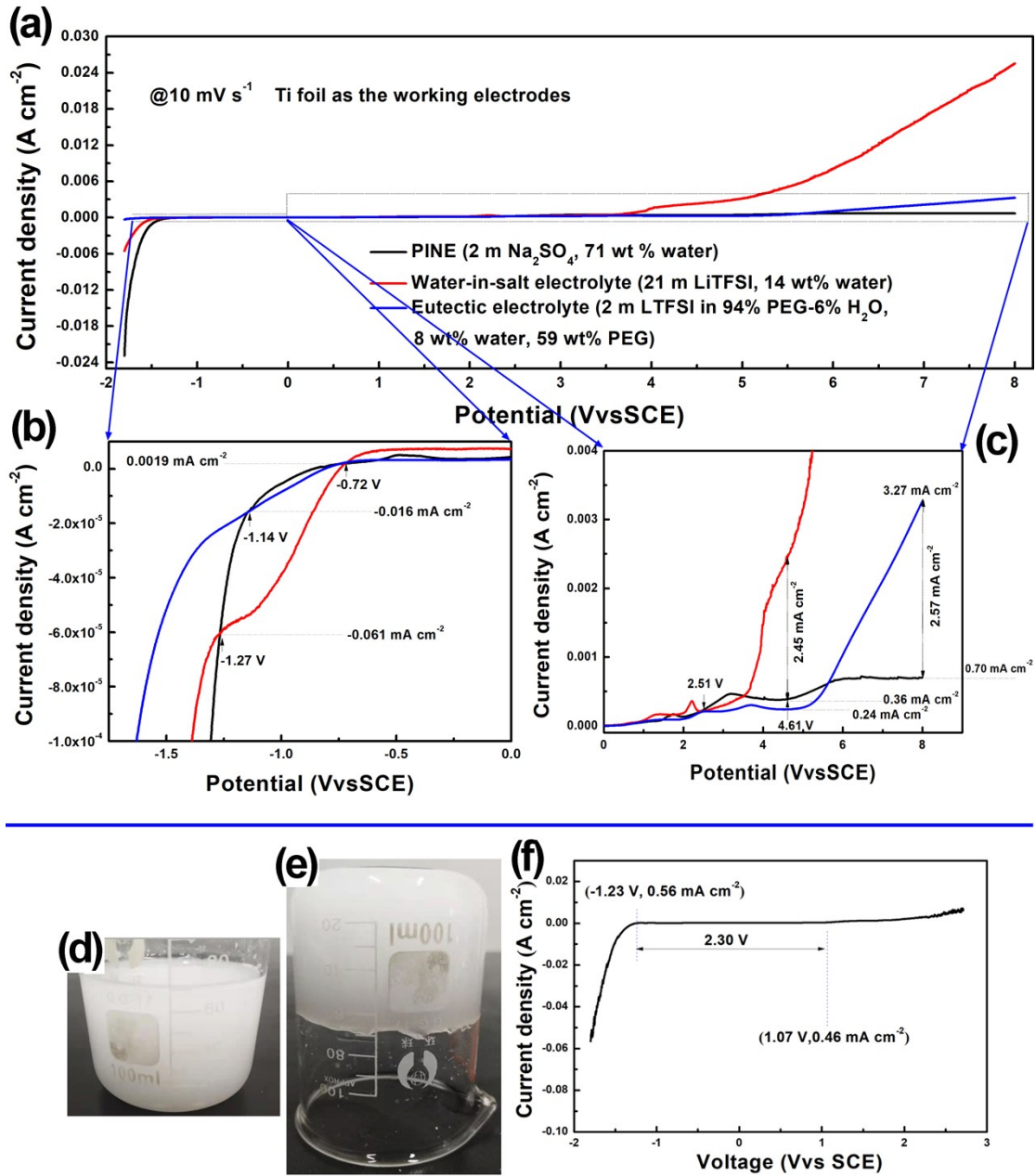
Figure S4 (a) LSV curves comparison of our PINE with water-in-salt electrolyte and eutectic electrolyte, and (b) and (c) partially enlarged curves. The optical photographs of (d) and (e) the white hydrogel obtained by replacing NaOH with 13.45 mL ammonia water, and (f) LSV curve. LSV of the white hydrogel obtained by replacing NaOH with 13.45 mL ammonia water. The ammonia reacts with $Al_2(SO_4)_3$ to form $Al(OH)_3$ gel, which shows a ~2.3 V ESW as shown in Figure S4(c), narrower than that of PINE one.
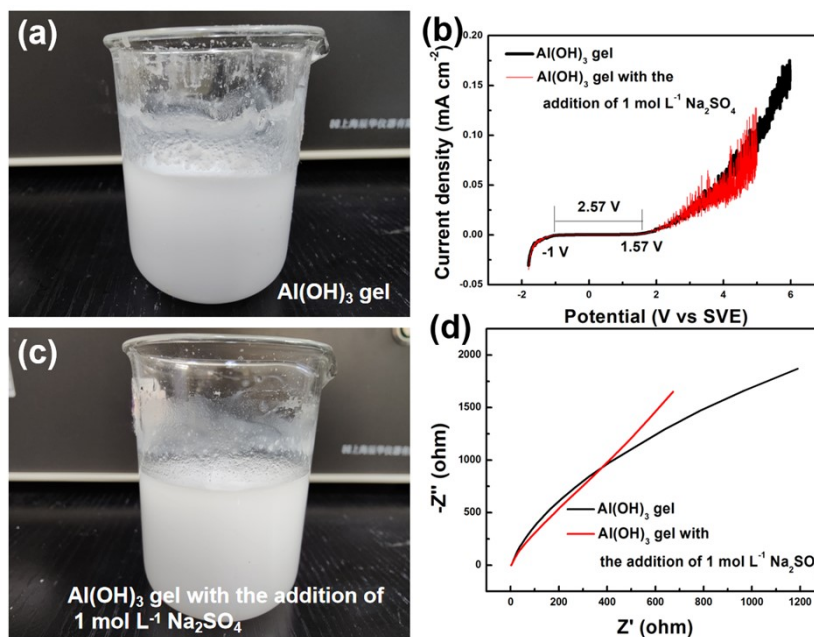
Figure S5 (a) and (c) The optical photographs, (b) LSV and (d) Nyquist plots for the Al(OH)$_3$ gel and the Al(OH)$_3$ gel with addition of 1 mol L^{-1} Na$_2$SO$_4$. Compared to PINE, both the Al(OH)$_3$ gel and the Al(OH)$_3$ gel with the addition of 1 mol L^{-1} Na$_2$SO$_4$ show narrower ESWs, although have higher ionic conductivities (120 mS cm^{-1} and 174 mS cm^{-1}, respectively). The addition of 1 M Na$_2$SO$_4$ could not result in the coagulation of Al(OH)$_3$ sol and the gelation.
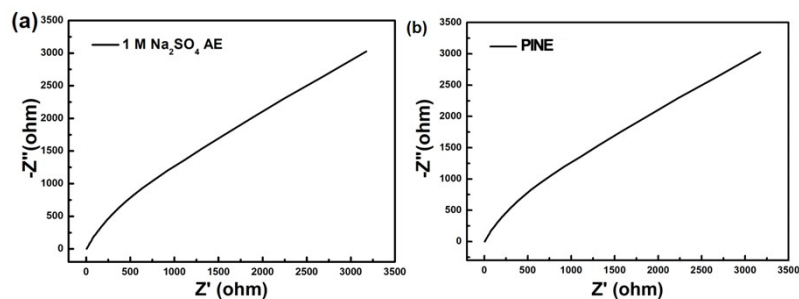
Figure S6 Nyquist plots of (a) 1 M Na$_2$SO$_4$ AE and (b) PINE. The electrolyte is sandwiched by the two platinum plates connected with the positive and negative electrodes.
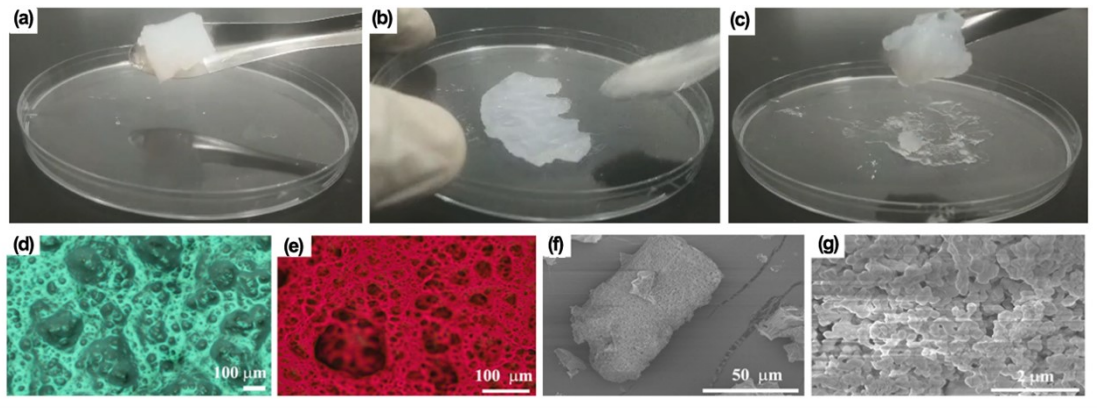
Figure S7 (a), (b), and (c) The optical images of PINE. (d) and (e) The optical microscope images of PINE. (f) and (g) SEM images of PINE.
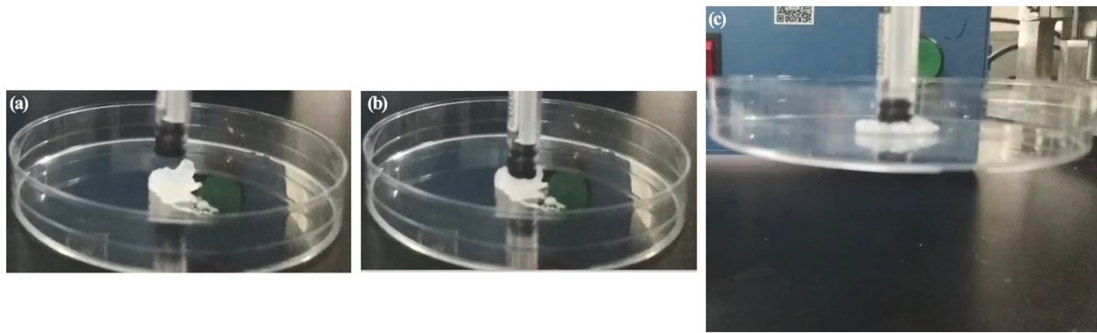

Figure S8 The optical images of viscous show for PINE. PINE (1.32 g) can paste the petri dish (6.32 g) and the ball-point pen (6.12 g) together.
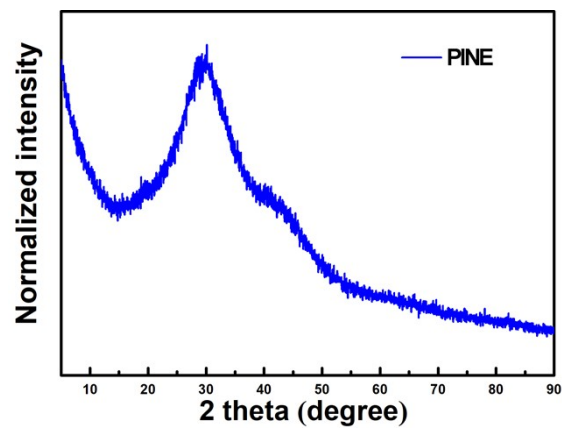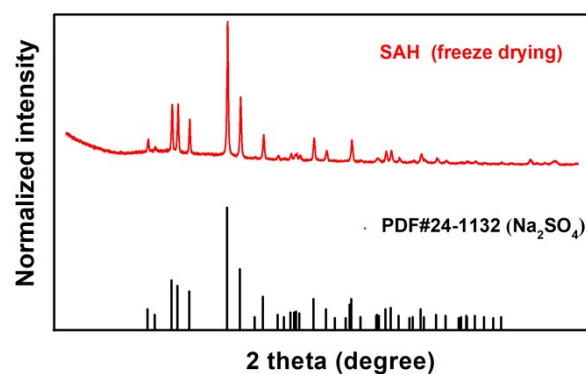

Figure S9 XRD pattern of PINE.

Figure S10 XRD curve of SAH (freeze drying) prepared using the method same as the PINE without the pre-addition of Na_2SO_4 (thenardite).
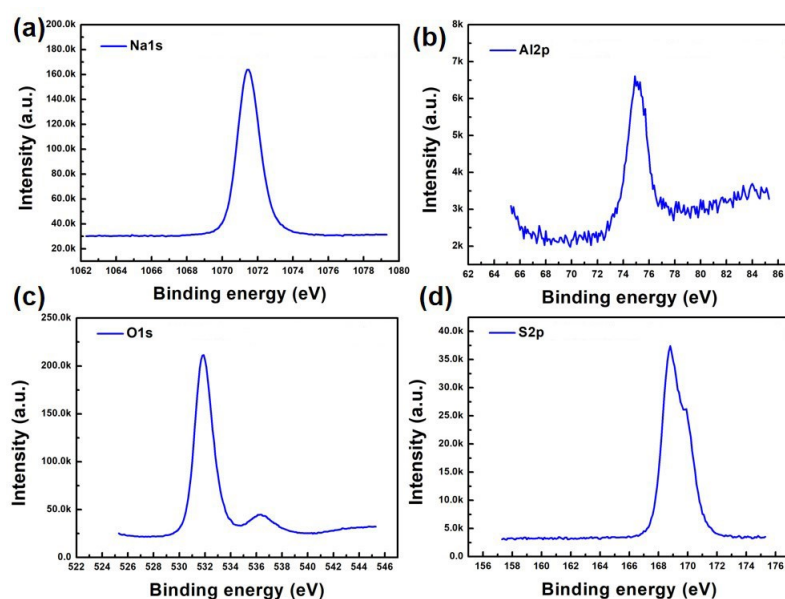

Figure S11 The narrow spectra of PINE (freeze drying) for (a) Na1s, (b) Al2p, (c) O1s, and (d)S2p.

The atom ratio of Na/Al is about 3.11:1 (229036/1.685:8435/0.193). The atom ratio of S/O is about 1:3.89 (73044.8/0.668:332199.4/0.78). The atom ratio of Na/Al is about 3:1.
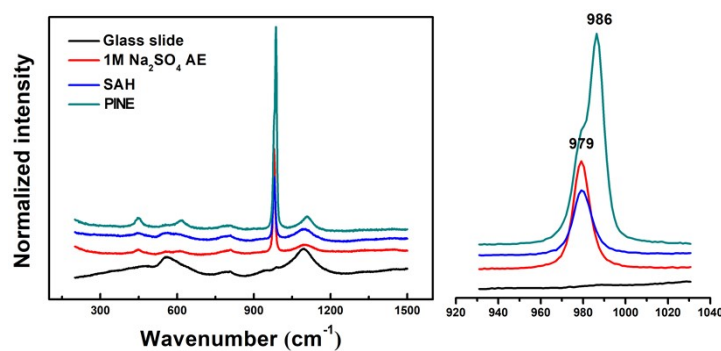

Figure S12 Raman patterns of 1 M Na_2SO_4 AE, SAH, and PINE. The glass slide is the substrate during the Raman test. The wavenumbers at 450 cm^{-1}, 617 cm^{-1}, 979 cm^{-1}, and 986 cm^{-1} belong to the v_1 SO_4^{2-} symmetric stretching.[7,]
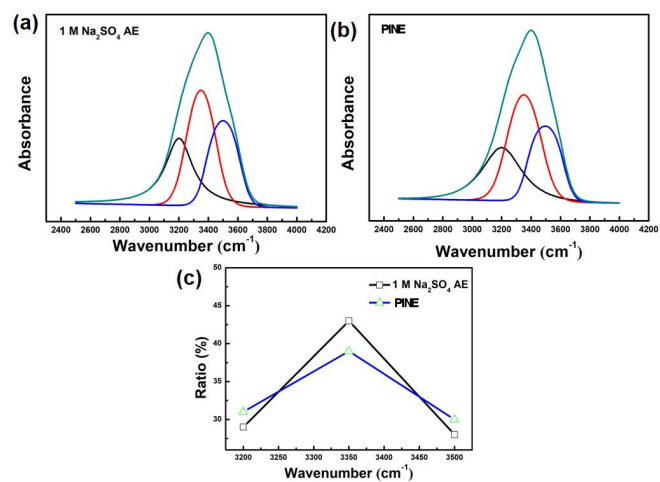
Figure S13 The peaks (2500~4000 cm⁻¹) differentiating analysis of ATR-FTIR for (a) 1 M Na$_2$SO$_4$ AE, SAH, and PINE. (d) The ratio of different hydrogen-bonded O-H in water.[7, 9]
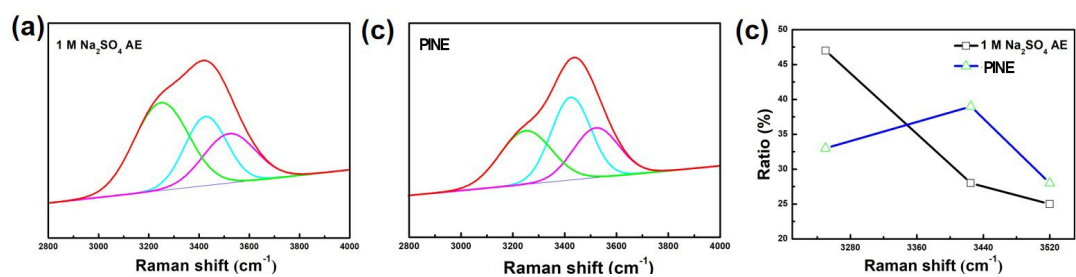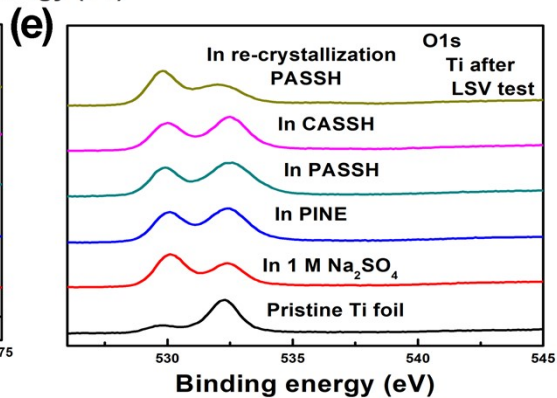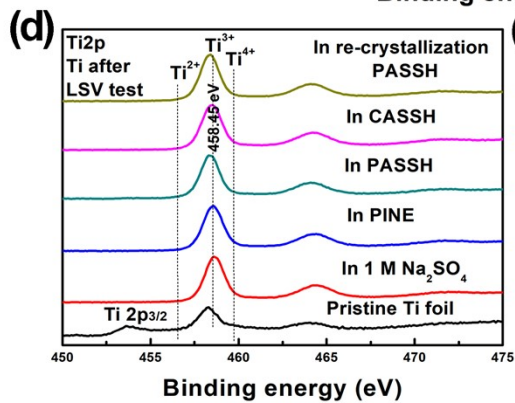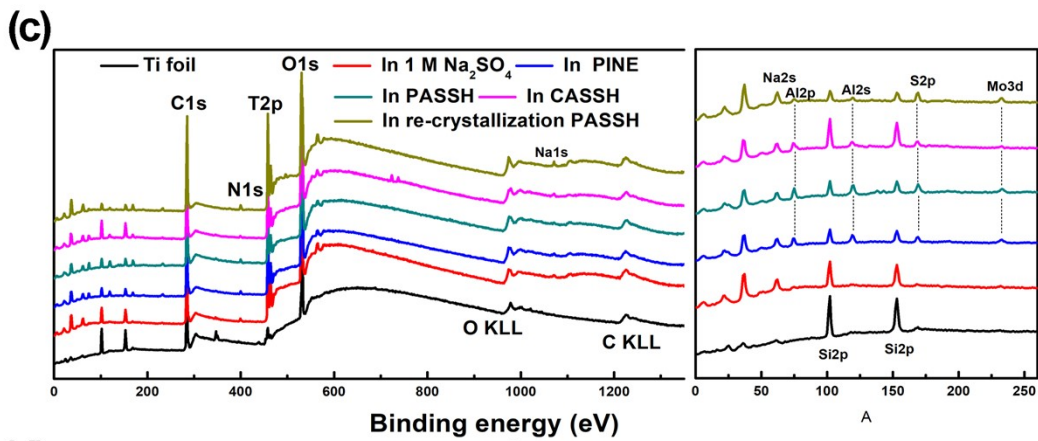

Figure S14 The peaks differentiating analysis of Raman for (b) 1 M Na$_2$SO$_4$ AE and PINE. (c) The ratio of three Raman peaks.[7, 9]

(a)

(b) Ti after LSV test in different electrolytes
- In re-crystallization PASSH
- In CASSH
- In PASSH
- In PINE
- In 1 M Na₂SO₄ AE
- Ti foil
- Ti   PDF#44-1294

2 theta (degree)

(c)
— Ti foil   — In 1 M Na₂SO₄   — In PINE
— In PASSH   — In CASSH
— In re-crystallization PASSH

C1s   T2p   O1s   N1s   Na1s   O KLL   C KLL

Binding energy (eV)

Na2s   Al2p   Al2s   S2p   Mo3d   Si2p   Si2p

Binding energy (eV)   A

(d) Ti2p   Ti³⁺
Ti after   Ti²⁺   Ti⁴⁺
LSV test
- In re-crystallization PASSH
- In CASSH
- In PASSH
- In PINE
- In 1 M Na₂SO₄
- Pristine Ti foil
458.45 eV
Ti 2p3/2

Binding energy (eV)

(e)   O1s
In re-crystallization   Ti after
PASSH   LSV test
- In CASSH
- In PASSH
- In PINE
- In 1 M Na₂SO₄
- Pristine Ti foil

Binding energy (eV)

Ti as the work electrodes after LSV test

(f)   (g)   (h)

In PINE   In water-in-salt electrolyte   In eutectic electrolyte

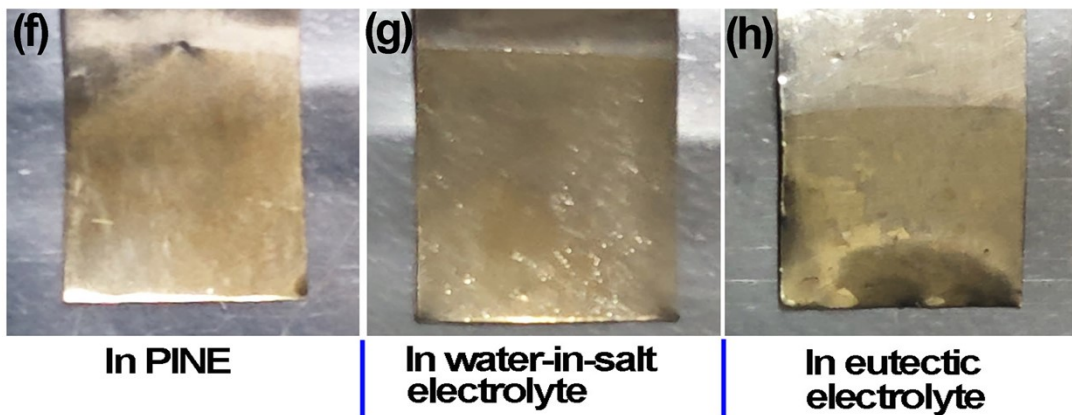**Figure S15** (a) The optical images of Ti electrodes after LSV test in different electrolytes, and the optical images correspond to (b) XRD patterns one by one. XPS spectra: (c) Ti2p and (d) O1s of Ti electrodes after LSV test in different electrolytes. The optical images of Ti as the working electrodes after LSV test in (f) PINE, (g) water-in-salt electrolyte and (h) eutectic electrolyte.

SEI with earthy yellow on the surface of Ti electrodes in our designed electrolytes

XPS and XRD characterizations are carried out for Ti electrodes after LSV test in electrolytes of 1 M Na_2SO_4 AE, PINE, PASSH, CASSH and Re-crystallization PASSH. After LSV test, compared with the Ti foil (without LSV test), the earthy yellow film is observed on the surface of Ti electrodes as shown in Figure S15(a), in which the optical images correspond to XRD patterns of Figure S15(b) one by one.

XRD pattern is employed to investigate the Ti electrodes after LSV test as shown in Figure S15(b). Excluding the characteristic peaks of Ti foil (PDF#44-1294), no other peak is observed may due to (1) the earthy yellow film is amorphous; (2) the earthy yellow film is too thin to detect.

XPS is selected to further study the surface of Ti electrodes, in which the Ti foil with the purity of 99.999 wt% contains the elements of N, O, Si, Mo and so on with low content (we consulted the manufacturer). Figure S15(c) is the full and the partial enlarged spectra. The signal peaks of C1s, Ti2p and O1s are observed in Figure S15(c), in which the peak of C1s is used for the calibration. Also, the signal peaks of Si2p and Na1s are observed in XPS spectrum.[10, 11] Although the earthy yellow film is formed on the surface of Ti foil tested in all of electrolytes, some difference is still observed as shown in the partial enlarged spectra of Figure S15(c). Compared to Ti electrode after LSV test in 1 M Na_2SO_4 AE (red spectrum), the new signal peaks of Mo3d, S2p and Al (Al2s and Al2p) are observed in the partial enlarged spectra of Ti electrodes after LSV test in electrolytes of PINE, PASSH, CASSH and Re-crystallization PASSH.[12-14] The main composition of earthy yellow film is still Ti and O. Thus, the narrow spectra of Ti2p and O1s are collected. Black spectrum in Figure S15(d) is Ti2p of Ti foil.[15] After LSV test in the different electrolytes using Ti as the electrodes, the signal peak of Ti^{3+} is detected.[15, 16] The black spectrum in Figure S27(e) is O1s of Ti foil, in which the peaks at about 530 eV and 532 eV represent the oxygen from the natural TiO_2 and the surface species such as hydroxides, respectively.[17] The intensity of peaks at about 530 eV increases relatively compared to peaks at about 532 eV, indicating the relatively increased content of Ti_3O_2.

From the above analysis, (1) the SEI with earthy yellow on the surface of Ti electrode after LSV test in 1 M Na_2SO_4 AE composes of Ti, O, Na, Si, and N elements, which does not expand ESW; (2) the SEI with earthy yellow on the surface of Ti electrode after LSV test in PINE, PASSH, CASSH and re-crystallization PASSH composes of S, Al and Mo, together with Ti, O, Na elements, which can expand ESW.

Thus, the mechanism of our designed PINE on expanding ESW may be due to:

(1) the earthy yellow SEI on the surface of Ti electrodes;

The SEI may consist of the aluminium oxide and the sulfonate (R-SO$_3$X) from the reduction of SO_4^{2-}, which is as the following discussion in Figures S32, 33 and 34.

(2) the strong adsorption of PINE to water molecules, which is discussed in the submitted manuscript.

As shown in the Figures S15 (f, g, h), after LSV tests in PINE and the reported electrolytes (water-in-salt electrolyte published in Science; eutectic electrolyte published in Nature Materials), the earthy yellow films (complex in-situ products: LiF-containing compounds mixed with TiOx) are also observed on Ti surfaces, indicating the wide ESWs are contributed by the complex in-situ products. "The complex in-situ product" is also observed on Ti after LSV test in the dilute aqueous electrolytes, but shows a narrow ESW. The complex in-situ products result in the wide or narrow ESWs, which are caused by the properties differences between PINE, water-in-salt electrolytes, eutectic electrolytes and dilute aqueous electrolyte.
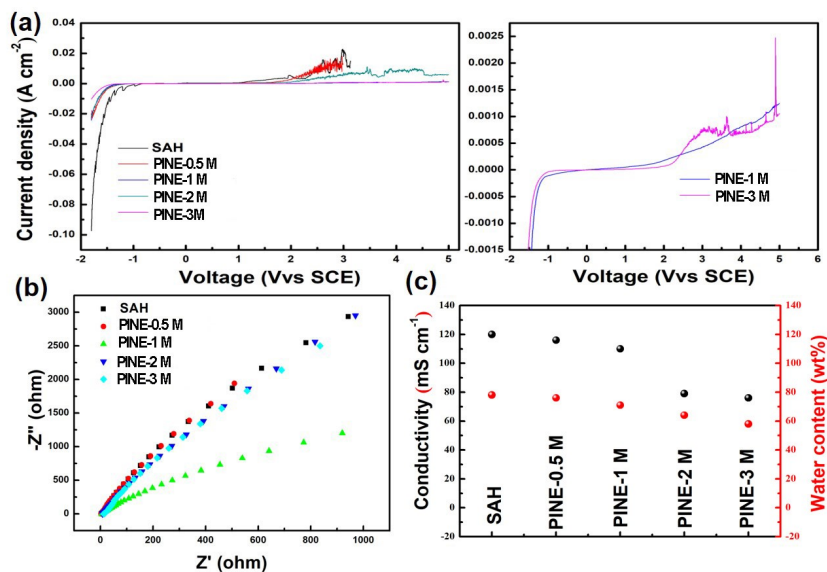
Figure S16 The effect of Na$_2$SO$_4$ concentration on the physicochemical properties of PINE. (a) LSV curves at a scan rate of 10 mV s^{-1}. SAH represents the addition of 0 M Na$_2$SO$_4$. PINE-0.5 M represents the addition of 0.5 M Na$_2$SO$_4$. PINE-1 M (PINE) represents the addition of 1 M Na$_2$SO$_4$. PINE-2 M represents the addition of 2 M Na$_2$SO$_4$. PINE-3 M represents the addition of 3 M Na$_2$SO$_4$. (b) Nyquist plots, the electrolyte is sandwiched by the platinum plates connected with the positive and negative electrodes. (c)Variations of conductivity and water content with the change of Na$_2$SO$_4$ concentration.
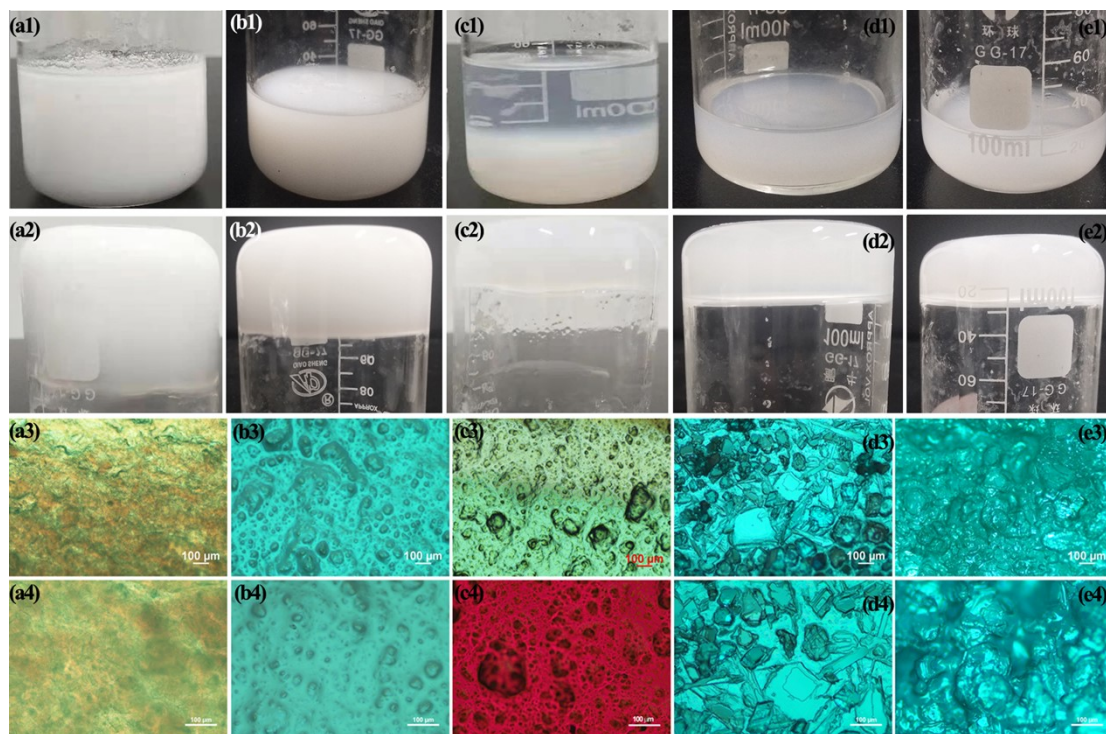

Figure S17 The optical images for (a1) and (a2) SAH, (b1) and (b2) PINE-0.5 M, (c1) and (c2) PINE-1 M, (d1) and (d2) PINE-2 M, (e1) and (e2) PINE-3 M. The optical microscope images of (a3) and (a4) for SAH, (b3) and (b4) for PINE-0.5 M, (c3) and (c4) for PINE-1 M, (d3) and (d4) for PINE-2 M, (e3) and (e4) for PINE-3 M.

The effect of Na_2SO_4 concentration on the physicochemical properties of PINE electrolyte is investigated (e.g., ESW, ionic conductivity, and so on). The concentration of 0 M, 0.5 M, 1 M, 2 M, and 3 M Na_2SO_4 is selected and the electrolytes are denoted as SAH, PINE-0.5 M, PINE-1 M (PINE), PINE-2 M, and PINE-3 M, respectively. As shown in Figure S16(a), ESW increases from ~1.91 V for SAH, ~2.72 V for PINE-0.5 M, ~4.64 V for PINE-1 M, ~3 V for PINE-2 M, and ~4.66 V for PINE-3 M. LSV curve of PINE-3 M shows a peak at ~3 V and a larger current density than that of PINE-1 M as shown in Figure S16(a). The ionic conductivity and the water content gradually decrease with the increased concentration of Na_2SO_4 in Figure S16(c). The optical images of these electrolytes exhibit a solid-state characteristic as shown in Figures S17 (a1 and a2, b1 and b2, c1 and c2, d1 and d2, e1 and e2). The optical microscope images are also recorded to detect the phase separation behavior of these electrolytes. No microstructure is observed for SAH in Figures S17(a3) and (a4). The pre-adding 0.5 M Na_2SO_4 into the aqueous solution, PINE-0.5 M appears an initial phase separation process with the cross-linked network but a low porosity in Figures S17 (b3) and (b4). Increasing the pre-addition concentration of Na_2SO_4, PINE-1 M exhibits an obvious phase separation process with the cross-linked network and high porosity in Figures S17 (c3) and (c4). The PINE-2 M and PINE-3 M show a fragmentation of network and are toward the transformation of the spheroidization and sedimentation in Figures S17 (d3) and (d4), S16(e3) and (e4). Without the pre-addition of Na_2SO_4 (thenardite), the prepared electrolyte (SAH) shows a liquid behavior, no phase separation process is observed as shown in Figure S18. It can be inferred that the phase separation and the coagulation are induced by the pre-addition of Na_2SO_4 (thenardite).
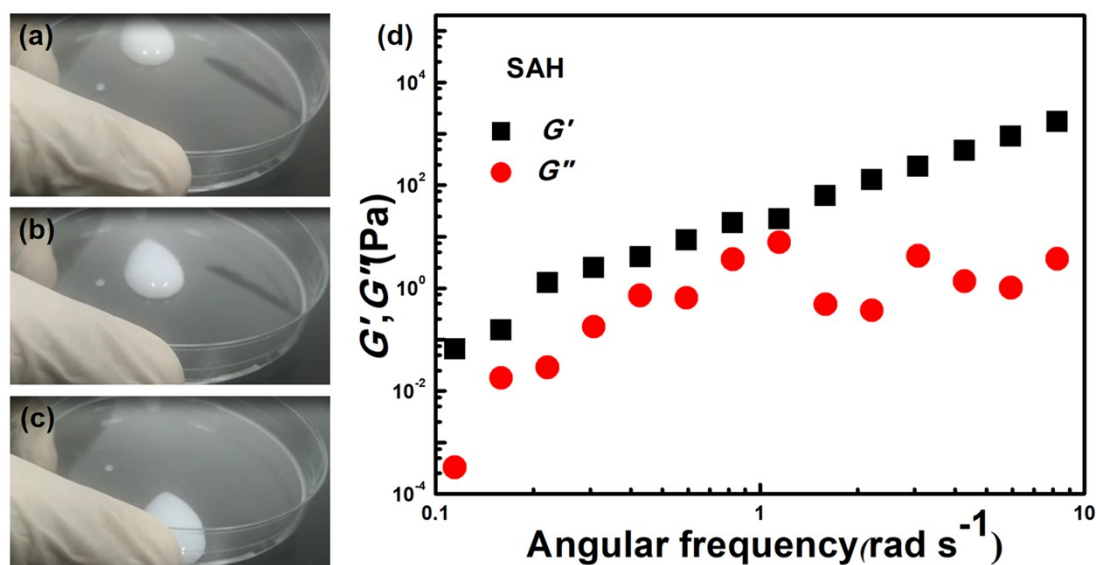

Figure S18 The optical images for (a), (b), and (c) SAH. The viscoelastic properties of SAH: the frequency dependence of the storage (G') and loss (G") modulis for (d) SAH.

A small part of "solid-state" SAH is poured into the plastic petri dish and depressed using the medicine spoon. The white liquid drop of SAH flows down when leaning the plastic petri dish as shown in Figures S18 (a), (b), and (c). Pristine SAH in beaker indicates a pseudo solid state (liquid) behavior. The viscoelastic properties of SAH care evaluated by the mechanical spectra at 26 °C. As shown in Figure S18(d), SAH shows a liquid-like behavior with an obvious dependence of G' and G" as a function of the angular frequency.
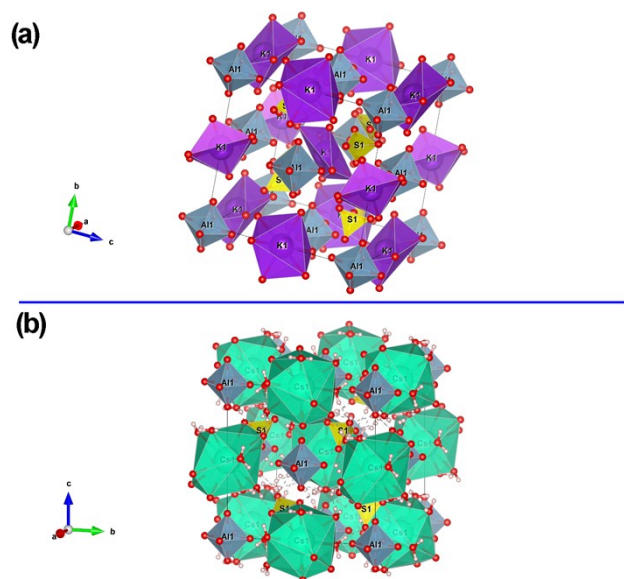
Figure S19 (a) The crystal structure of $KAl(SO_4)_2 \cdot 12H_2O$. The red ball represents oxygen, and the pink ball hydrogen. The earthy yellow ball (oxygen) connects with sulfur to form SO_4^{2-}. A sodium ion coordinates with 6 water molecules to form $K(H_2O)_6^+$ octahedron. An aluminium ion coordinates with 6 water molecules to form $Al(H_2O)_6^{3+}$ octahedron. (b) Crystal structure of $CsAl(SO_4)_2 \cdot 12H_2O$. The red ball represents oxygen, and the pink ball hydrogen. The earthy yellow ball (oxygen) connects with sulfur to form SO_4^{2-}. An aluminium ion coordinates with 6 water molecules to form $Al(H_2O)_6^{3+}$ octahedron.
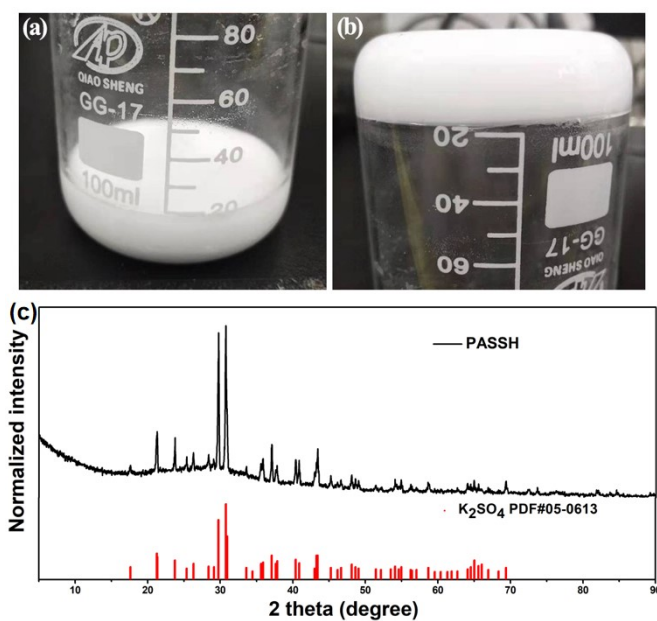

Figure S20 (a) and (b) The optical images of potassium alum (PASSH). (c) XRD pattern of PASSH.

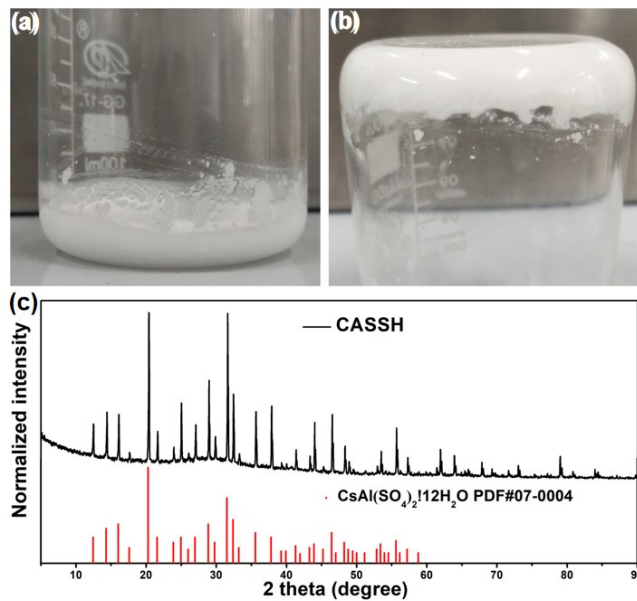**Figure S21** The optical images of (a) and (b) caesium alum (CASSH). (c) XRD pattern of CASSH.

Figure S22 LSV curves of PINE, PASSH and CASSH.
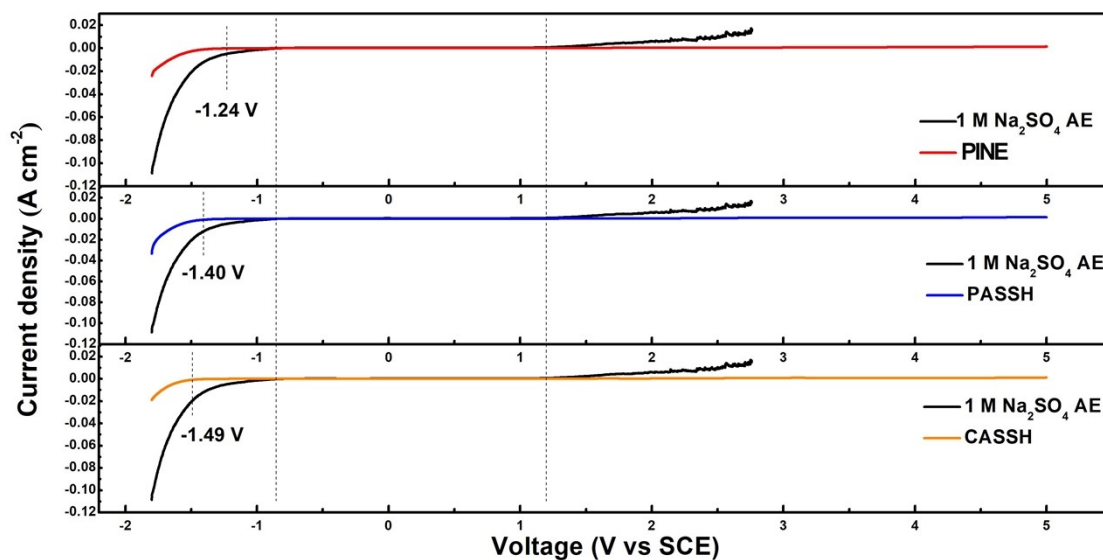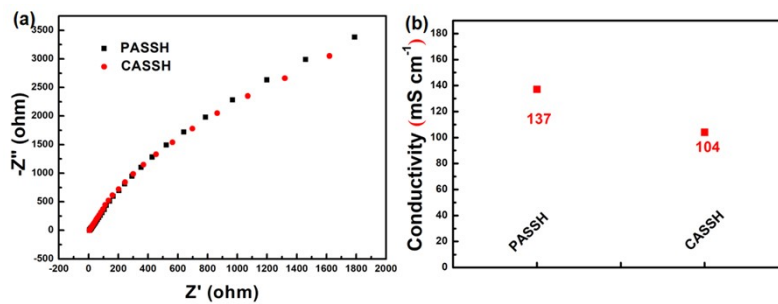

Figure S23 Nyquist plots of (a) PASSH and (b) CASSH. (c) The conductivities of PASSH and CASSH.
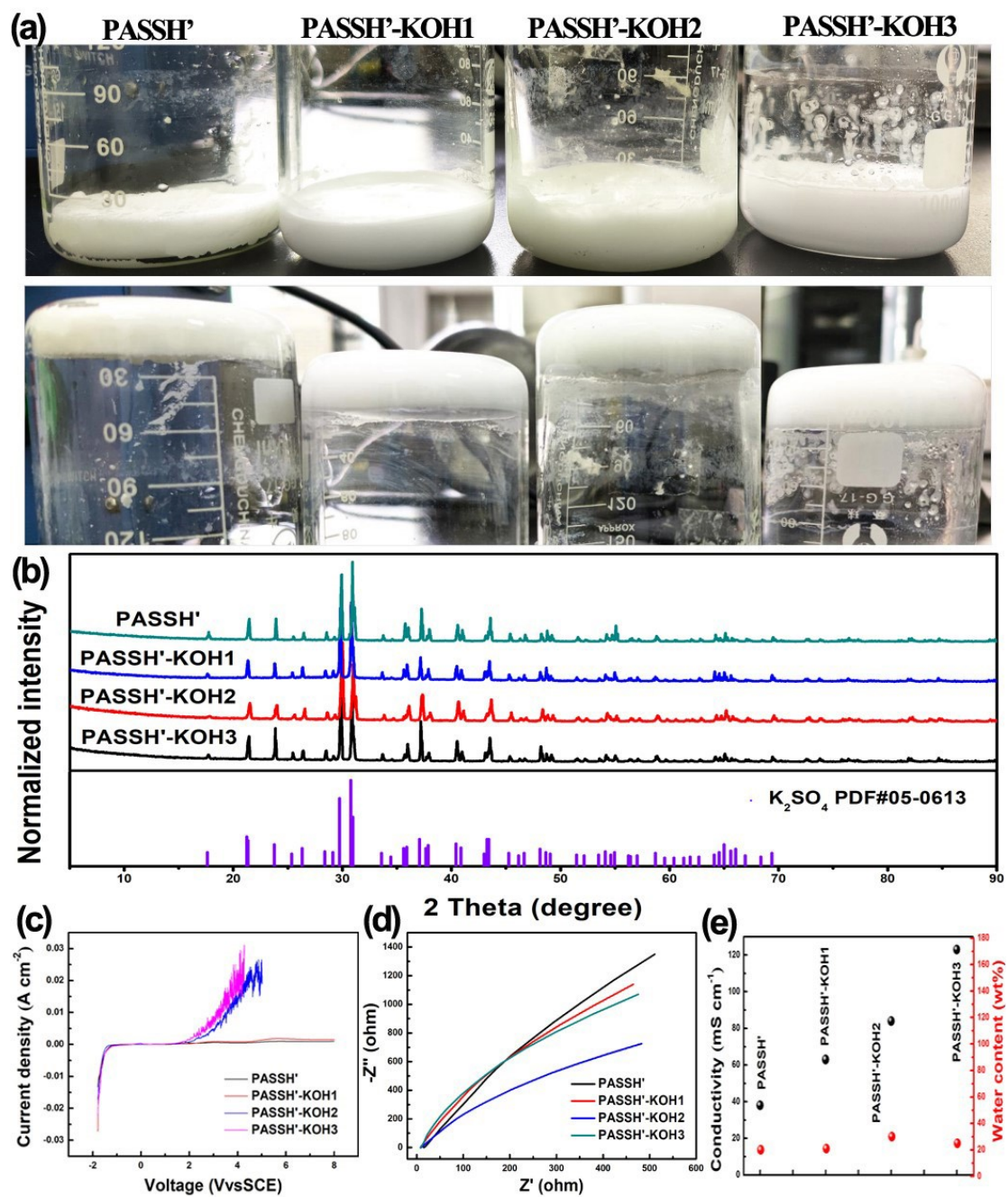
Figure S24 (a) The optical images and (b) XRD patterns of PASSH', PASSH'-KOH1, PASSH'-KOH2 and PASSH'-KOH3. (c) LSV curves of PASSH', PASSH'-KOH1, PASSH'-KOH2 and PASSH'-KOH3. (d) Nyquist plots and (e) the conductivity of PASSH', PASSH'-KOH1, PASSH'-KOH2 and PASSH'-KOH3.
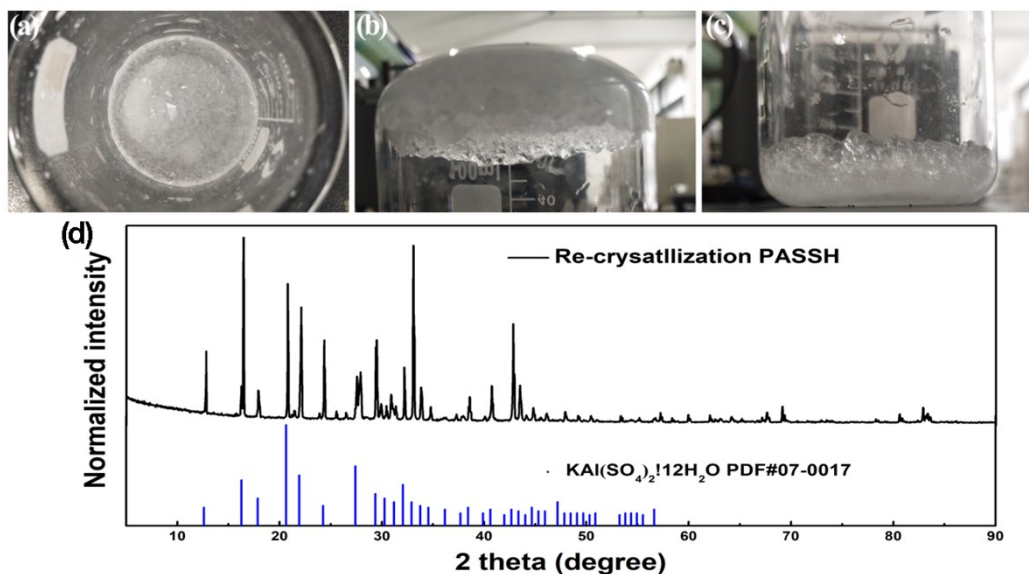
Figure S25 (a), (b), (c) The optical images and (d) XRD pattern of re-crystallization PASSH.

The crystallized electrolyte (re-crystallization PASSH) is prepared by dissolved 1 M K_2SO_4 and 0.72 M $KAl(SO_4)_2 \cdot 12H_2O$ into 60 mL deionized water with the temperature of 70 °C and then cooled at room temperature as shown in Figure S24. The re-crystallization PASSH is composed of the interconnected crystals as shown in Figures S24 (a, b, and c). XRD pattern exhibits the obvious diffraction peaks indexed to $KAl(SO_4)_2 \cdot 12H_2O$ (PDF#07-0017).
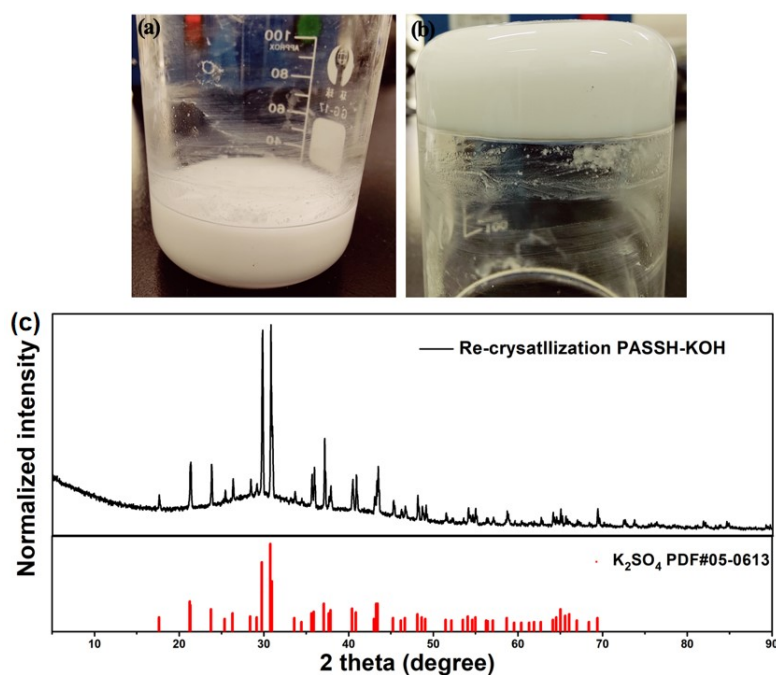
Figure S26 (a), (b) The optical images and (c) XRD pattern of re-crystallization PASSH-KOH.

Also, KOH dissolved into the precursor solution leads to the amorphous $KAl(SO_4)_2 \cdot 12H_2O$ electrolyte (re-crystallization PASSH-KOH) as displayed in Figure S25.
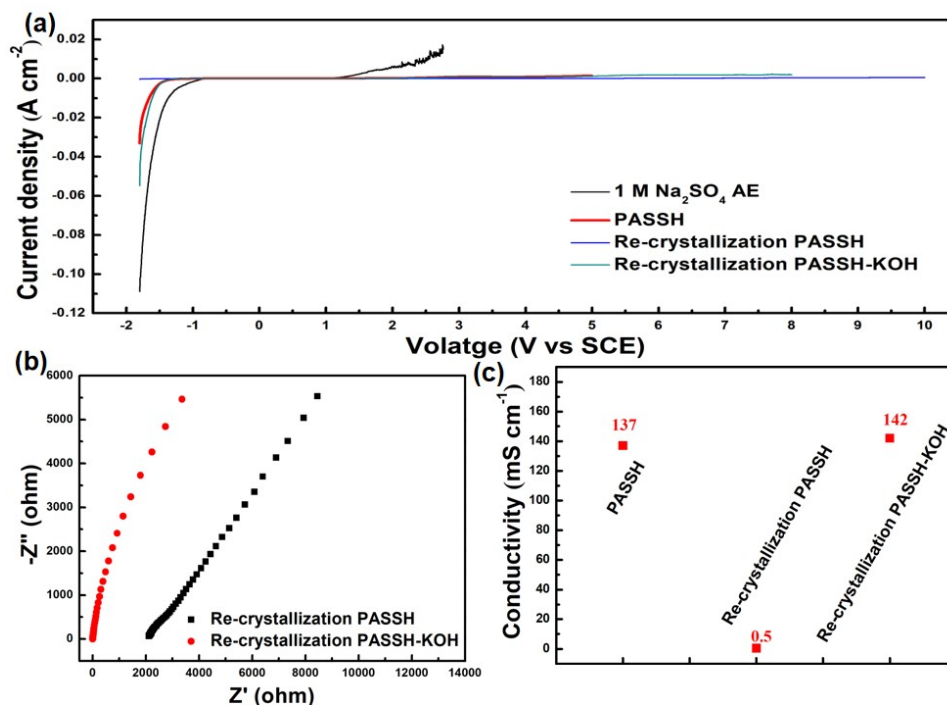
Figure S27 (a) LSV curves of re-crystallization PASSH-KOH, re-crystallization PASSH, PASSH and 1 M Na$_2$SO$_4$ AE. (b) Nyquist plots and (c) the conductivity.
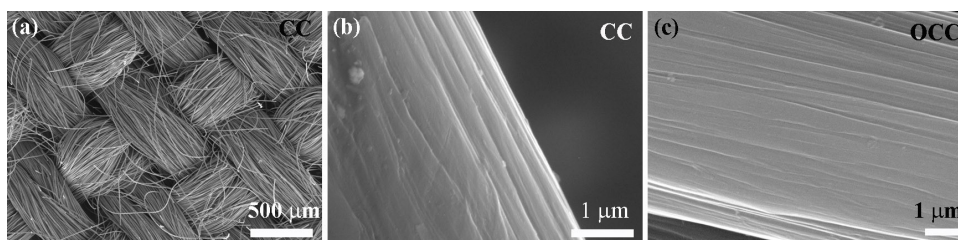
Figure S28 SEM images of (a), (b) CC, and (c) OCC, CC and OCC are also used as the electrodes of supercapacitors.[18]
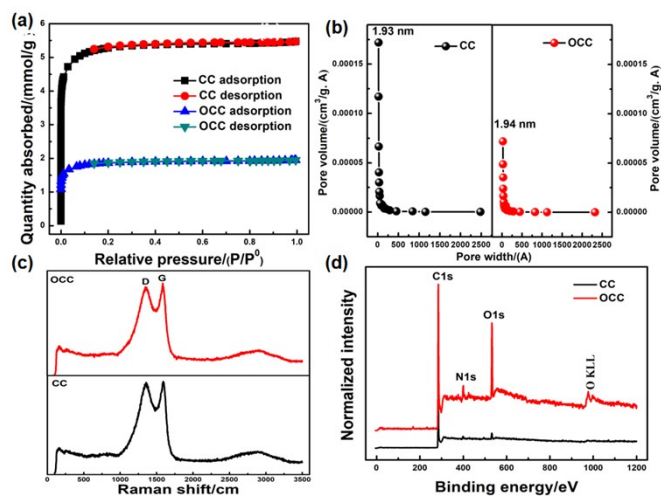
Figure S29 (a) The specific surface area plots, (b) pore width curves, (c) Raman spectra, and (d) XPS full spectra.

BET surface areas are 360 m^2 g^{-1} for CC and 127 m^2 g^{-1} for OCC, and pore volumes are 0.19 cm^3 g^{-1} for CC and 0.07 cm^3 g^{-1} for OCC. CC and OCC are also used as the electrodes of supercapacitors. [18]
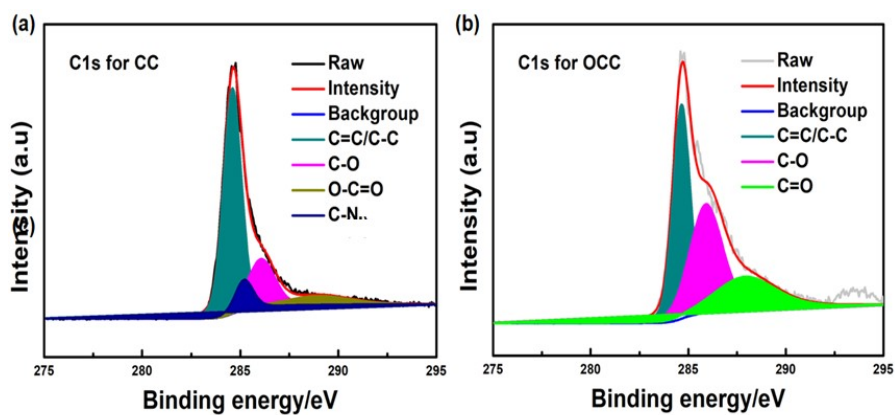
Figure S30 C1s narrow spectra for (a) CC and (b) OCC. CC and OCC are also used as the electrodes of supercapacitors. [18]

**Figure S31** The optical image of the solid-state supercapacitor (OCC//CC supercapacitor based on PINE). The solid-state supercapacitor is in-situ fabricated by immersing OCC and CC electrodes into the precursor solution of PINE, in which OCC and CC are sandwiched with the white PTFE electrode clips. And cycled for 1000 cycles with the voltage window of 0~2.1 V at a current density of 18 mA cm^{-2}. The area of CC and OCC is 1 cm^2. The supernatant has been poured out.

Figure S32 The electrochemical properties of OCC cycled in OCC//CC based on 1 M Na$_2$SO$_4$ AE and PINE. (a) CV curves at 10 mV s^{-1}, (b) the capacity as a function of current density and (c) Nyquist plots. The electrochemical properties of CC cycled in OCC//CC based on 1 M Na$_2$SO$_4$ AE and PINE. (d) CV curves at 10 mV s^{-1}, (e) the capacity as a function of the current density and (f) Nyquist plots.

The electrochemical properties of the cycled electrodes:

The electrochemical tests of the cycled electrodes were carried out to study the capacity degradation reason of OCC//CC based on 1 M Na$_2$SO$_4$ AE and the enhanced mechanism of OCC//CC based on PINE, as shown in Figure S32.

For the two OCC negative electrodes cycled in the supercapacitors, the electrochemical performances of OCC cycled in OCC//CC based on PINE decrease a little as shown in Figures S32(a) and (b), compared to OCC cycled in OCC//CC based on 1 M Na$_2$SO$_4$ AE. Nyquist plots are employed to further detect the resistance variations of the cycled CC electrodes as shown in Figu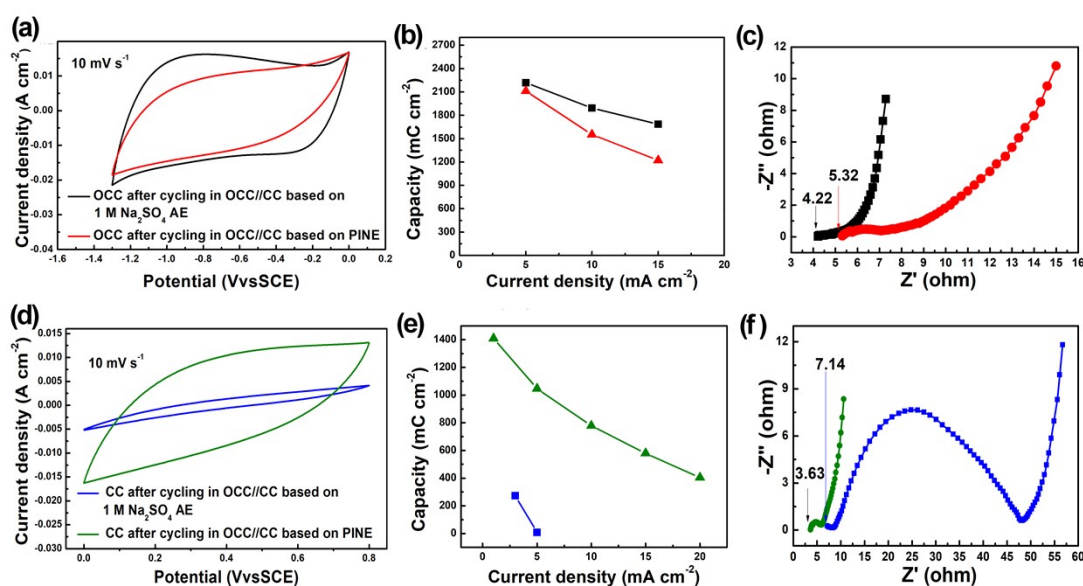re S32(c). *Res* of OCC cycled in OCC//CC based on PINE is 5.32 ohm, higher than that of OCC cycled in OCC//CC based on 1 M Na$_2$SO$_4$ AE. Also, a small semicircle is observed in the plot of OCC cycled in OCC//CC based on PINE, indicating an increased *Rct*. At the low-frequency region, smaller inclination angle is observed in the plot of OCC cycled in OCC//CC based on PINE. The decreased capacity of OCC cycled in OCC//CC based on PINE may be derived from the increased resistance.

For the electrochemical properties of the cycled CC positive electrodes in the two supercapacitors, as shown in Figure S32(d), CV curve of CC cycled in OCC//CC based on 1 M Na$_2$SO$_4$ AE presents a fusiform shape with a smaller integral area than that of CC cycled in OCC//CC based on PINE with the rectangular shape. As shown in Figure S32(e), the areal capacity of CC cycled in OCC//CC based on 1 M Na$_2$SO$_4$ AE only delivers 8 mC cm^{-2} at 5 mA cm^{-2}, significantly lower than that of CC cycled in OCC//CC based on PINE (1049 mC cm^{-2} at 5 mA cm^{-2}). Nyquist plots are employed to further reveal the resistance variations of the cycled CC electrodes as shown in Figure S32(f). *Res* and *Rct* of CC cycled in OCC//CC based on 1 M Na$_2$SO$_4$ AE are 7.14 ohm and 41.24 ohm, respectively, much larger than those of CC cycled in OCC//CC based on PINE. Thus, it can be concluded that the rapid capacity degradation and the resistance increases after 13000 cycles for OCC//CC based on 1 M Na$_2$SO$_4$ AE are due to the gradual capacity degradation and the resistance increases of CC positive electrodes during the frequently charging/discharging process. Positive carbon material enduring the high voltage of supercapacitor shows the capacity decay and the resistance increases due to the electro-oxidation and the pore blockage by the decomposers of electrolyte.[19-22] CC cycled in OCC//CC based on PINE keeps a high retention of initial capacity due to the avoiding of the electro-oxidation and the pore blockage by the decomposers of electrolyte.

For a supercapacitor, its capacity is determined by the electrode with the lowest capacity. For the cycled OCC//CC based on 1 M Na_2SO_4 AE, the capacity of cycled CC positive electrode decreased more than that of cycled OCC negative electrode. Thus, the poor capacity retention of OCC//CC based on 1 M Na_2SO_4 AE is due to the degradation of CC positive electrode. In other words, the enhanced capacity retention of OCC//CC based on PINE is due to the avoiding of the capacity degradation of CC positive electrode. PINE with wider ESW than that of 1 M Na_2SO_4 AE makes OCC//CC operate stably in a wider voltage window.
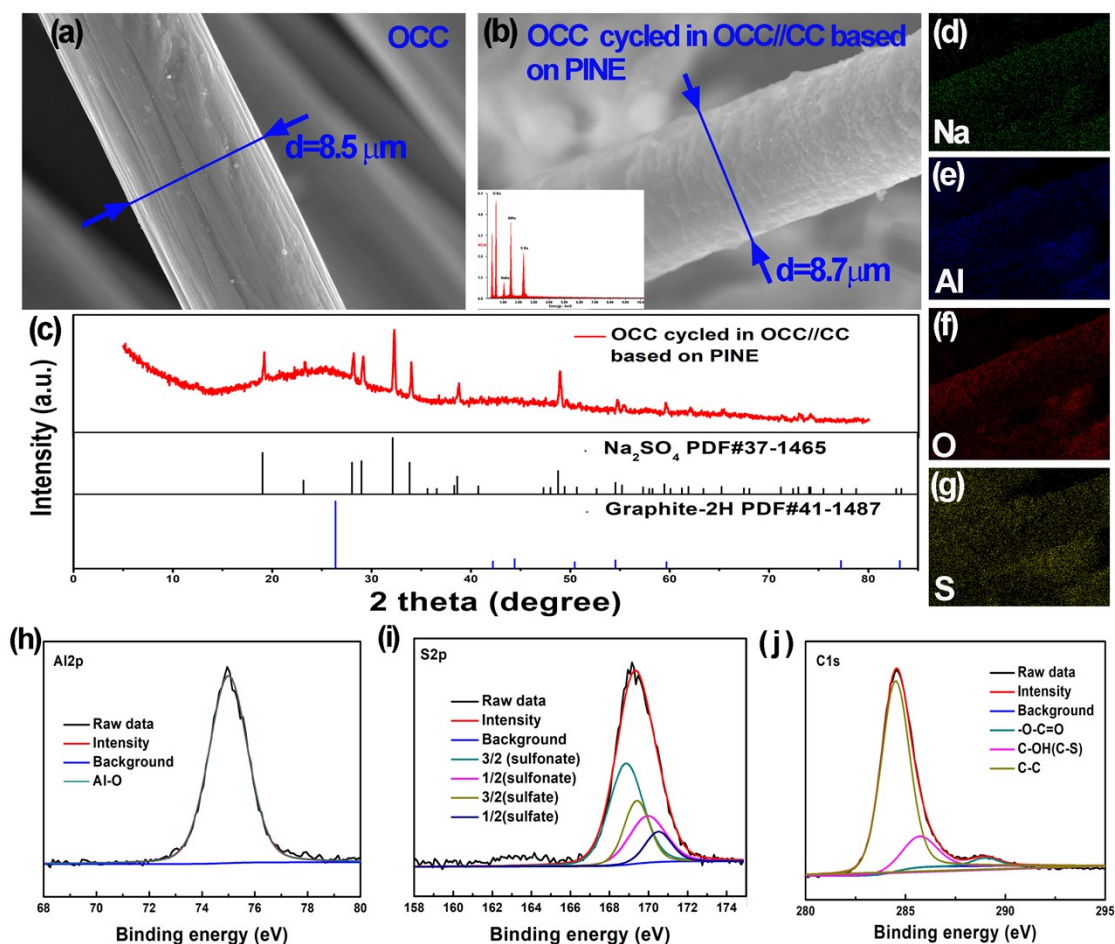
Figure S33 The characterizations on the solid electrolyte interphase (SEI) of OCC cycled in OCC//CC based on PINE. SEM images of (a) OCC and (b) OCC cycled in OCC//CC based on PINE, inset in the left bottom: EDAX with the C, Na, O, Al and S elements. (c) XRD pattern of OCC cycled in OCC//CC based on PINE. EDAX mapping images of (d) Na element, (e) Al element, (f) O element, (g) S element from Figure S33(b). XPS characterizations of OCC cycled in OCC//CC based on PINE: the narrow spectra of (h) Al2p, (i) S2p and (j) C1s.

The mechanism of PINE enhancing the capacity of OCC//CC is further investigated as the followings:

For the cycled OCC negative electrode, characterizations are carried out to investigate the reason as shown in Figure S33. Compared to the single carbon fiber of the pristine OCC in Figure S33(a), the carbon fiber of OCC cycled in OCC//CC based on PINE shows a larger diameter (~8.7μm) and rough surface in Figure S33(b), indicating the formation of solid state interphase (SEI). XRD pattern is collected to detect the phase of SEI as shown in Figure S33(c). Excluding the broad peaks at ~26° (carbon cloth, PDF#41-1487), the diffraction peaks are observed in the spectrum (red) of OCC cycled in OCC//CC based on PINE, which corresponds to Na_2SO_4 (PDF#37-1465). Excluding Na_2SO_4, other phase of SEI is not detected may due to the amorphous feature. Energy

dispersive x-ray analysis (EDAX) is carried out to investigate the component of SEI. As shown in Figures S33(d-g), Na, Al, S and O elements are observed, indicating SEI composes of Na, S, Al and O elements. XPS is selected to investigate the SEI as shown in Figures S33(h-j). The Al2p, S2p, and C1s spectra are fitted by Gaussian fitting method. As shown in Figure S33(h), the binding energy at 74.95 eV is consistent with Al-O bond, indicating the existence of aluminium oxide (e.g., Al_2O_3).[23] The binding energies at 169.4 and 170.5 eV in Figure S33(i) are S2p3/2 and S2p1/2, respectively, which are corresponding to sulfate (Na_2SO_4).[24] The binding energies at 168.85 and 169.95 eV in Figure S33(i) are S2p3/2 and S2p1/2, respectively, which are corresponding to sulfonate (R-SO_3X, R and X are unknown), and this indicates that S is reduced together with the decreased valence state from +6 of SO_4^{2-} to +5 of R-SO_3X.[24-26] The binding energy at 285.7 eV in Figure S33(j) may belong to C-S bond, indicating R in R-SO_3X may be carbon.[27] One can conclude that SEI may consist of aluminium oxide, Na_2SO_4 and sulfonate (R-SO_3X). SEI with earthy yellow on Ti electrode may contain aluminium oxide and sulfonate (R-SO_3X), which can expand ESW. It is difficult to further investigate the mechanism of SEI on expanding ESW due to the complexity of SEI composition. On the one hand, the increased resistance in Figure S32(c) may due to the formation of SEI. On the other hand, SEI servers as an electron barrier preventing the reduction of water while allowing Na^+ migration. Also, the decreased current density in Figure 4(d) especially at -1.3 V may be due to the existence of SEI preventing the reduction of water, resulting in an expanded voltage window. SEI on the negative electrode cycled in aqueous batteries using "water-in-salt" aqueous electrolyte is observed.[28]
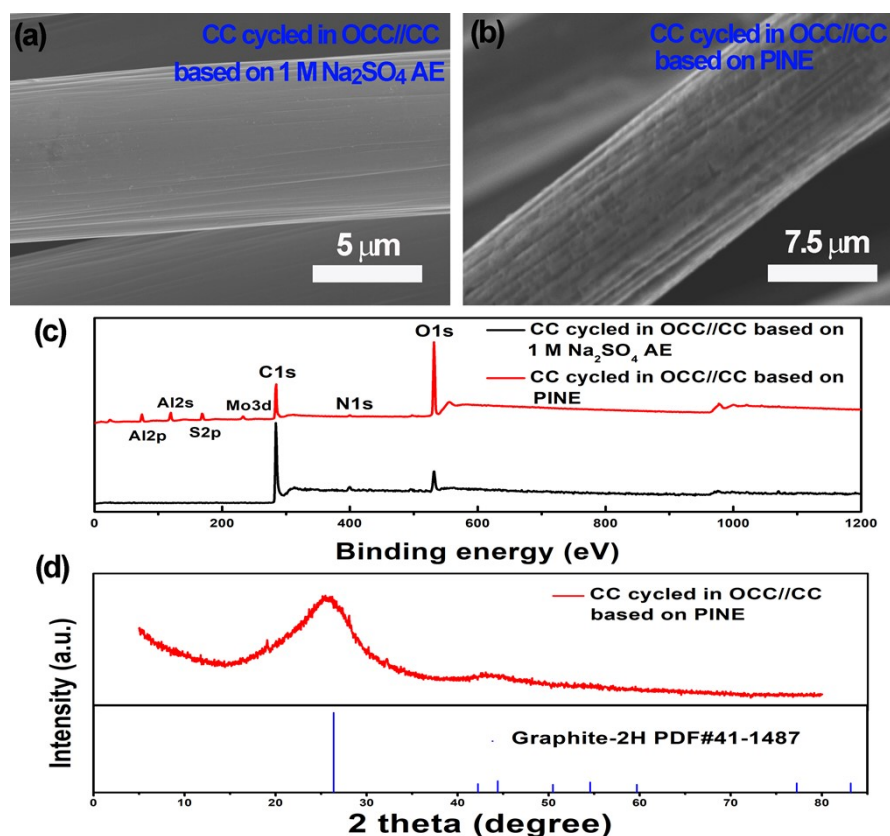
Figure S34 SEM and XPS of CC cycled in OCC//CC based on 1 M Na_2SO_4 AE and PINE. (a) and (b) SEM images. (c) XPS spectra. (d) XRD of CC cycled in OCC//CC based on PINE.

For the cycled CC positive electrodes, SEM and XPS characterizations are made as shown in Figure S34. Compared to CC cycled in OCC//CC based on 1 M Na_2SO_4 AE (Figure S34a), the cathode electrolyte interphase (CEI) is observed on the surface of carbon fiber as shown in Figure S34(b). Figure S34(c) is XPS spectra.

Compared to the black spectrum (CC cycled in OCC//CC based on 1 M Na_2SO_4 AE), the new peaks of S2p, Al2p and Al2s are observed in the red spectrum (CC cycled in OCC//CC based on PINE), excluding the signal peaks of C1s, N1s and O1s from carbon fiber. The signal peak of Mo3d is derived from carbon cloth ("the residual Mo was from the sizing agent during the preparation process", the manufacturer said). The composition of CEI contains the elements of S, Al, and O, and may consist of aluminium oxide and sulfonate (R-SO_3X). XRD pattern is collected as shown in Figure S34(d). Excluding the signal peak at ~26° (carbon cloth, PDF#41-1487), no other peak is detected may due to the amorphous feature of CEI. The CEI (1) servers as an electron barrier preventing the oxidation of water while allowing ions migration, and (2) avoids the capacity degradation of CC positive electrode during the charging/discharging process.

Based on the above analysis in Figures S32, 33 and 34, the mechanism of PINE enhancing the capacity of OCC//CC after long-term cycles is as the followings:

the CEI and SEI are formed on the surface of CC and OCC during the cycling process, respectively, which could avoid the oxidation and the reduction of water and thus enhance the capacity retention of OCC//CC.
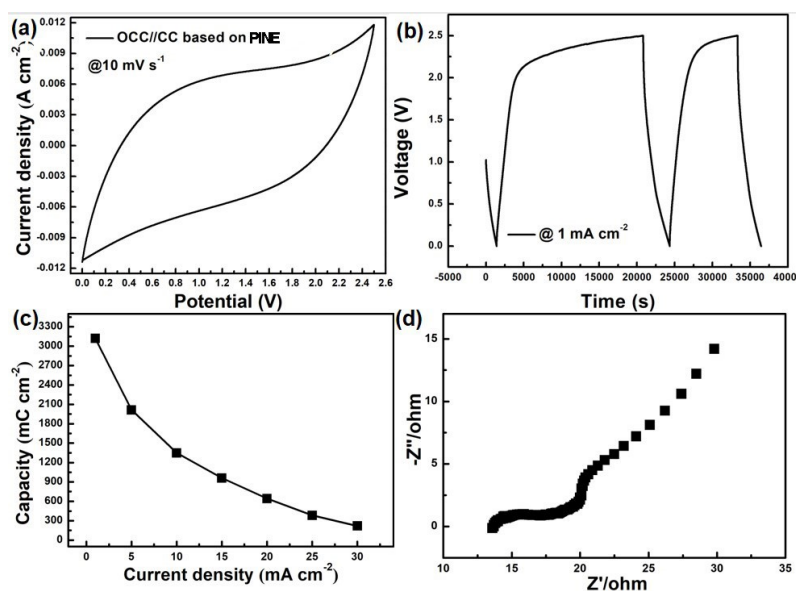
Figure S35 The electrochemical properties of OCC//CC supercapacitor based on PINE after 10000 cycles. (a) CV curve. (b) GCD curve. (c) The capacity as a function of the current density. (d) Nyquist plot.
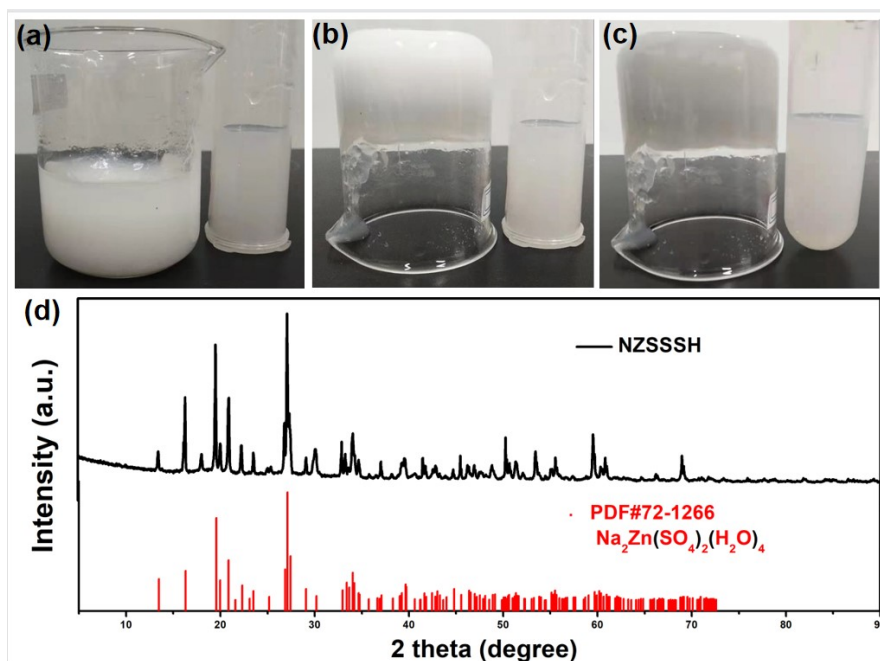
Figure S36 (a), (b), and (c) The optical images of NZSSSH at the bottom of beaker. NZSSSH is prepared by replacing 1 M Na_2SO_4 with 1 M Zn_2SO_4 with the same parameters as PINE. NZSSSH is located at the bottom of beaker. (d) XRD pattern of NZSSSH dried at 60 °C in an oven.
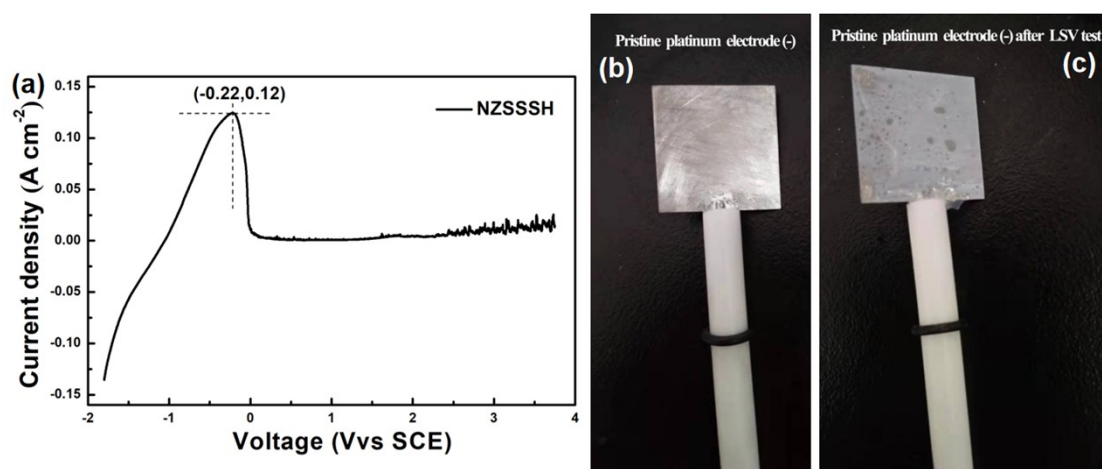
Figure S37 (a) LSV curve of NZSSSH in a three-electrode configuration at a scan rate of 10 mV s^{-1}, in which Pt plate, Ti plate, and SCE are used as counter electrode, working electrode, and reference electrode, respectively. The optical images of Pt plates (b) before and (c) after LSV tests.

Compared to the pristine Pt electrode, a zinc film is deposited on the surface of Pt plate after LSV test, demonstrating there is a reaction of Zn^{2+} and Zn. Thus, NZSSSH as the electrolyte is coupled with CC (+) and OCC (-) to form a zinc ion hybrid supercapacitor.
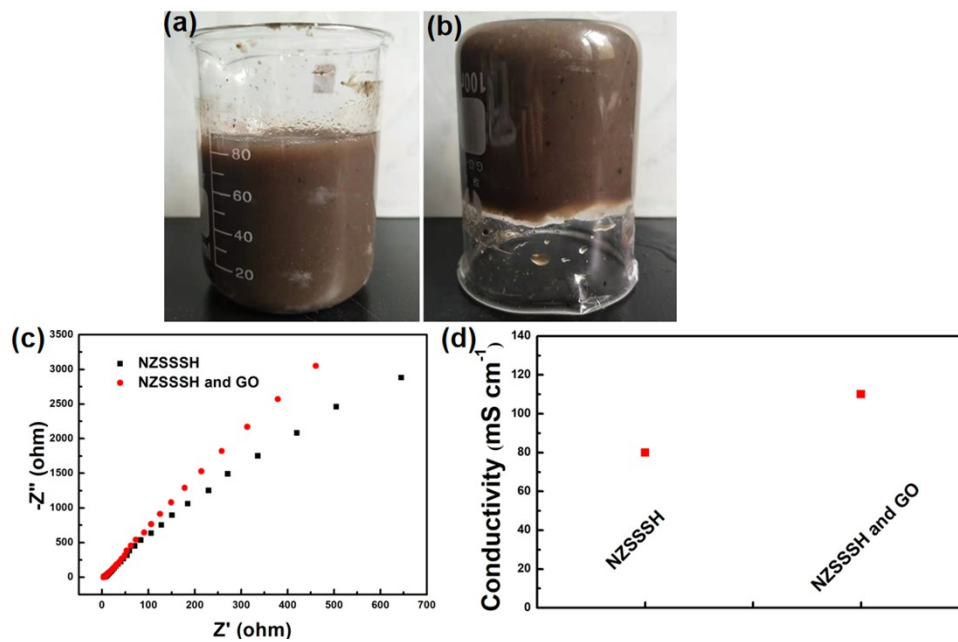
Figure S38 (a) The optical images of NZSSSH and GO. (b) Nyquist plots of NZSSSH, (b) NZSSSH and GO. (d) The conductivities of NZSSSH, NZSSSH and GO.
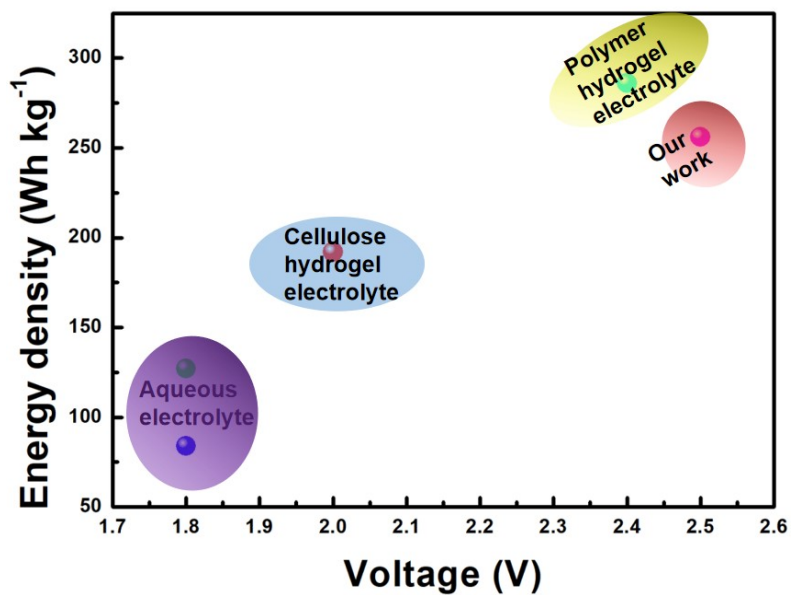
Figure S39 The comparisons of the electrochemical properties of the reported zinc ion hybrid supercapacitors with our work based on Table S3.
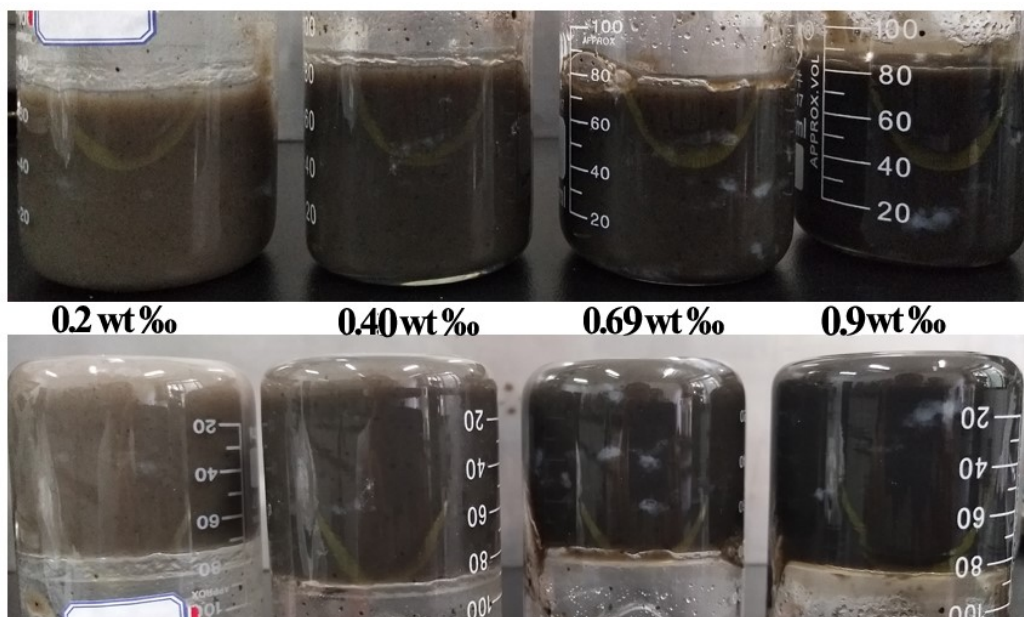
Figure S40 The optical images of NZSSSH and GO electrolytes with the different GO contents. 0.2 wt‰ represents the GO content is 0.2% in a thousand.

Figure S41 (a) Nyquist plots of NZSSSH and GO with the different GO content. (b) Conductivities of NZSSSH and GO with the different GO contents. (c) LSV curves of NZSSSH and GO electrolytes with the different GO contents.

Part 3. Tables

Table S1 Conductivities, ESW and water content of our prepared electrolytes

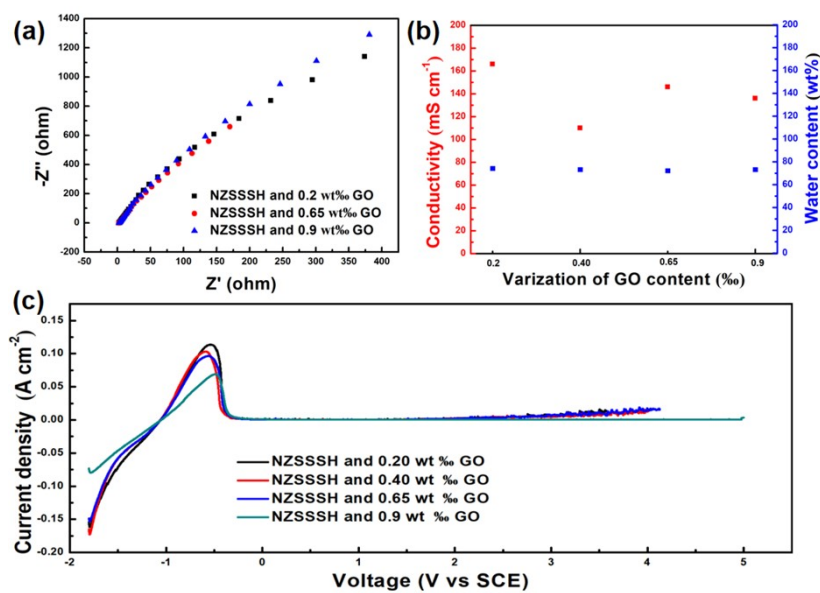| Electrolytes	H(cm)	R(ohm)	A (cm²)	Conductivity (mS cm⁻¹)	ESW (V)	Water content (wt%)
Quasi-solid-state electrolyte of transparent crystal sheets	1.25	12.75	3.4	29	about 2.56	above 55
Single transparent crystal sheet	0.05	1200	0.04×0.04	26	~	55
1 M Na₂SO₄ AE	0.90	4.30	1.68	125	about 2.02	87
SAH	1.5	3.04	4	120	about 1.8	78
PINE-0.5 M	1.3	2.8	4	116	about 2.7	76
PINE-1 M (PINE)	1.3	4.3	2.8	110	about 4.6	71
PINE-2 M	1.3	7.41	2.2	79	about 2.7	64
PINE-3 M	1.3	12.1	1.4	76	about 4.64	58
Re-crystallization PASSH	1.3	2116	1.2	0.5	about 11.6	Do not measure
PASSH	1.35	6.80	1.45	137	about 4.6	Do not measure
CASSH	1.2	5.75	2	104	about 4.6	Do not measure
Re-crystallization PASSH-KOH	1.3	3.15	2.9	142	about 4.6	Do not measure
NZSSSH	1.65	4.08	4	80	~	Do not measure
NZSSSH and 0.20 wt‰ GO	1.6	2.4	4	116	~	74
NZSSSH and 0.40 wt‰ GO (NZSSSH and GO)	1.65	3.6	4	110	~	73
NZSSSH and 0.65wt‰ GO	1.35	2.3	4	79	~	72
NZSSSH and 0.90 wt‰ GO	1.2	2.2	4	76	Expanded ESW	73
PASSH'	1.2	15	2.1	38	About 4.6	20
PASSH'-KOH1	0.95	7.5	2	63	About 4.6	21
PASSH'-KOH2	1.55	9.2	2	84	About 2.8	30
PASSH'-KOH3	1.35	7.7	1.43	123	about 2.8	25

Conductivity is based on the formula: $\delta = H/(R \times A)$,[29] H is the vertical distance between two platinum plates, R is the resistance from the intercept of plots and Z' axis, A is the area of platinum inserted into the electrolyte.

Table S2 Synthesis parameters of our electrolytes

Electrolytes	Weight of Al$_2$(SO$_4$)$_3$·18H$_2$O (g)	Weight of alkali (g)	Weight of sulfate (g)	Weight of H$_2$O (g)	Weight of GO (mL)	Weight of alum (M or g)
Quasi-solid-state electrolyte of transparent crystal sheets	8.16	0	12.90(Na$_2$SO$_4$)	38.56	0	0
1 M Na$_2$SO$_4$ AE	0	0	8.61(Na$_2$SO$_4$)	60	0	0
SAH	14.40	4(NaOH)	0	60	0	0
PINE-0.5 M	14.40	4(NaOH)	4.30(Na$_2$SO$_4$)	0	0	0
PINE-1 M (PINE)	14.40	4(NaOH)	8.60(Na$_2$SO$_4$)	60	0	0
PINE-2 M	14.40	4(NaOH)	17.20(Na$_2$SO$_4$)	60	0	0
PINE-3 M	14.40	4(NaOH)	25.8(Na$_2$SO$_4$)	60	0	0
Re-crystallization PASSH	0	0	10.56(K$_2$SO$_4$)	60	0	0.72M
PASSH	14.40	5.441(KOH)	10.56(K$_2$SO$_4$)	60	0	0
CASSH	14.40	16.97(CsOH·H$_2$O)	21.73(Cs$_2$SO$_4$)	60	0	0
Re-crystallization PASSH-KOH	0	5.44(KOH)	10.56(K$_2$SO$_4$)	60	0	0.72M
NZSSSH	14.40	4(NaOH)	10.77(ZnSO$_4$·H$_2$O)	60	0	0
NZSSSH and 0.20 wt‰ GO	14.40	4(NaOH)	10.77(ZnSO$_4$·H$_2$O)	65.5	5	0
NZSSSH and 0.40 wt‰ GO (NZSSSH and GO)	14.40	4(NaOH)	10.77(ZnSO$_4$·H$_2$O)	60	10.5	0
NZSSSH and 0.65wt‰ GO	14.40	4(NaOH)	10.77(ZnSO$_4$·H$_2$O)	54	16.5	0
NZSSSH and 0.90 wt‰ GO	14.40	4(NaOH)	10.77(ZnSO$_4$·H$_2$O)	47.20	23.30	0
PASSH'	1.2	0(KOH)	38.2(K$_2$SO$_4$)	57	0	4.8g
PASSH'-KOH1	0.95	0.64(KOH)	38.2(K$_2$SO$_4$)	57	0	4.8g
PASSH'-KOH2	1.55	1.40(KOH)	38.2(K$_2$SO$_4$)	57	0	4.8g
PASSH'-KOH3	1.35	2.80(KOH)	38.2(K$_2$SO$_4$)	57	0	4.8g

Note: the other parameters and the details are included in experimental section (Part 1).

Table S3 Comparisons of the electrochemical properties of the reported zinc ion hybrid supercapacitors with our work [30-33]

PE	NE	E	VW(V)	C (mAh g^{-1})	E (Wh kg^{-1})	R
Activated carbon	Zinc foil	Cellulose hydrogel	2	193	192	30
Carbon cloth	Zinc foil	Zn$_2$SO$_4$ aqueous electrolyte	1.8	156	127	31
Activated carbon	Zinc foil	Zn$_2$SO$_4$ aqueous electrolyte	1.8	121	84	32
Activated carbon	Zinc foil	Natural polymer hydrogel	2.4	260	286	33
CC	OCC	NZSSSH and GO	2.5	205	256	Our work

PE represents the positive electrode, NE represents the negative electrode, E represents the electrolyte, VW represents the voltage window, C represents the capacity, E represents the energy density, and R represents the reference.

Table S4 Elements content in PINE and PASSH based on ICP-OES

Elements	Elements content in PINE (mg kg^{-1})	Elements	Elements content in PASSH (mg kg^{-1})
Na	194259.26	K	300450.11
Al	30148.15	Al	4570.52

The mass ratio of Na$_2$SO$_4$ vs NaAl(SO$_4$)$_2$·12H$_2$O is 1:1 for PINE. The mass ratio of K$_2$SO$_4$ vs KAl(SO$_4$)$_2$·12H$_2$O is 8:1 for PASSH.

Table S5 Interacting energy of the different species from the simulating computation and literatures

Type	Binding energy(kJ mol^{-1})	Type	Binding energy(kJ mol^{-1})
Na$^+$-H$_2$O (hydration)	-405	Al(H$_2$O)$_6$$^{3+}$-H$_2$O(adsorption)	-228
SO$_4$$^{2-}$-H$_2$O (hydration)	-140	Na(H$_2$O)$_6$$^+$-H$_2$O(adsorption)	-26
H$_2$O-H$_2$O(hydrogen-bond)	-21	Al(H$_2$O)$_6$$^{3+}$-SO$_4$$^{2-}$(adsorption)	1.34
		Na(H$_2$O)$_6$$^{3+}$-SO$_4$$^{2-}$(adsorption)	about 1.34

Note: 1 eV is equal to 96 kJ mol^{-1}.

The left is from the reported literatures,[34-36] and the right from our simulating computation. Na$^+$-H$_2$O (hydration) represents the adsorption of Na$^+$ to H$_2$O and is from the primary solvation sheath of Na$^+$. SO$_4$$^{2-}$-H$_2$O (weak hydration) represents the adsorption of SO$_4$$^{2-}$ to H$_2$O and is from the primary solvation sheath of SO$_4$$^{2-}$. H$_2$O-H$_2$O (hydrogen-bond) represents the adsorption of H$_2$O to H$_2$O and is from the bulk water.

Al(H$_2$O)$_6$$^{3+}$-H$_2$O represents the adsorption of Al(H$_2$O)$_6$$^{3+}$ to H$_2$O and is from poly(ions-H$_2$O ligand) network of PINE. Na(H$_2$O)$_6$$^+$-H$_2$O the adsorption of Na(H$_2$O)$_6$$^+$ to H$_2$O and is from poly(ions-H$_2$O ligand) network of PINE. Al(H$_2$O)$_6$$^{3+}$-SO$_4$$^{2-}$(adsorption) represent the adsorption of Al(H$_2$O)$_6$$^{3+}$ site to SO$_4$$^{2-}$ of ions/H$_2$O hydrogen-bond network. Na(H$_2$O)$_6$$^+$-SO$_4$$^{2-}$(adsorption) represent the adsorption of Al(H$_2$O)$_6$$^{3+}$ site to SO$_4$$^{2-}$ of "ions/H$_2$O hydrogen-bond network".

References

1.   G. Kresse and J. Furthmüller, *Computational Materials Science*, 1996, **6**, 15-50.

2.   G. Kresse and J. Furthmüller, *Physical Review B*, 1996, **54**, 11169-11186.

3.   P. E. Blöchl, *Physical Review B*, 1994, **50**, 17953-17979.

4.   G. Kresse and D. Joubert, *Physical Review B*, 1999, **59**, 1758-1775.

5.   K. Perdew Jp Fau - Burke, M. Burke K Fau - Ernzerhof and M. Ernzerhof.

6.   Z. Deng, Z. Zhu, I.-H. Chu and S. P. Ong, *Chemistry of Materials*, 2016, **29**, 281-288.

7.   A. J. Locke, W. N. Martens and R. L. Frost, *Journal of Raman Spectroscopy*, 2007, **38**, 1429-1435.

8.   K. Ben Mabrouk, T. H. Kauffmann, H. Aroui and M. D. Fontana, *Journal of Raman Spectroscopy*, 2013, **44**, 1603-1608.

9.   S. Cai, X. Chu, C. Liu, H. Lai, H. Chen, Y. Jiang, F. Guo, Z. Xu, C. Wang and C. Gao, *Advanced materials*, 2021, **33**, e2007470.

10.   M. Wang, Y. Zi, J. Zhu, W. Huang, Z. Zhang and H. Zhang, *Chemical Engineering Journal*, 2021, **417**, 129265.

11.   W. Wei, Y. Liu, X. Yao and R. Hang, *Surface and Coatings Technology*, 2020, **397**, 125907.

12.   X. Zhang, T. Ma, T. Fang, Y. Gao, S. Gao, W. Wang and L. Liao, *Journal of Alloys and Compounds*, 2020, **818**, 152821.

13.   X.-l. Wei, Y. Xia, X.-m. Liu, H. Yang and X.-d. Shen, *Electrochimica Acta*, 2014, **136**, 250-256.

14.   X. Cheng, L.-H. Rong, P.-F. Cao and R. Advincula, *ACS Applied Nano Materials*, 2021, **4**, 1394-1400.

15.   R. L. Kurtz and V. E. Henrich, *Surface Science Spectra*, 1998, **5**, 179-181.

16.   M.-S. Wong, H. Pang Chou and T.-S. Yang, *Thin Solid Films*, 2006, **494**, 244-249.

17.   T. Sultana, G. L. Georgiev, G. Auner, G. Newaz, H. J. Herfurth and R. Patwa, *Applied Surface Science*, 2008, **255**, 2569-2573.

18.   T. Qin, Z. Xu, Z. Wang, S. Peng and D. He, *Journal of Materials Chemistry A*, 2019, **7**, 26011-26019.

19.   Q. Gao, L. Demarconnay, E. Raymundo-Piñero and F. Béguin, *Energy & Environmental Science*, 2012, **5**, 9611.

20.   M. He, K. Fic, E. Frąckowiak, P. Novák and E. J. Berg, *Energy Environ. Sci.*, 2016, **9**, 623-633.

21.   P. Ratajczak, K. Jurewicz, P. Skowron, Q. Abbas and F. Béguin, *Electrochimica Acta*, 2014, **130**, 344-350.

22.   P. Ratajczak, K. Jurewicz and F. Béguin, *Journal of Applied Electrochemistry*, 2013, **44**, 475-480.

23.   L.-X. Tian, F. Zhang, Z.-W. Shen, G.-G. Yan, X.-F. Liu, W.-S. Zhao, L. Wang, G.-S. Sun and Y.-P. Zeng, *Chinese Physics B*, 2016, **25**, 128104.

24.   M. M. Figueira, B. Volesky and H. J. Mathieu, *Environmental Science & Technology*, 1999, **33**, 1840-1846.

25.   H. Wang, S. Wen, G. Han and Q. Feng, *Separation and Purification Technology*, 2019, **228**, 115756.

26.   Y. Wei, X. Ling, L. Zou, D. Lai, H. Lu and Y. Xu, *Colloids and Surfaces A: Physicochemical and*

Engineering Aspects, 2015, **482**, 507-513.

27.   C. Zu and A. Manthiram, *Advanced Energy Materials*, 2013, **3**, 1008-1012.

28.   L. Suo, O. Borodin, T. Gao, M. Olguin, J. Ho, X. Fan, C. Luo, C. Wang and K. Xu, *Science*, 2015, **350**, 938.

29.   L. Fang, Z. Cai, Z. Ding, T. Chen, J. Zhang, F. Chen, J. Shen, F. Chen, R. Li, X. Zhou and Z. Xie, *ACS Appl Mater Interfaces*, 2019, **11**, 21895-21903.

30.   L. Yang, L. Song, Y. Feng, M. Cao, P. Zhang, X.-F. Zhang and J. Yao, *Journal of Materials Chemistry A*, 2020, **8**, 12314-12318.

31.   Y. Li, W. Yang, W. Yang, Z. Wang, J. Rong, G. Wang, C. Xu, F. Kang and L. Dong, *Nano-Micro Letters*, 2021, **13**.

32.   L. Dong, X. Ma, Y. Li, L. Zhao, W. Liu, J. Cheng, C. Xu, B. Li, Q.-H. Yang and F. Kang, *Energy Storage Materials*, 2018, **13**, 96-102.

33.   L. Han, H. Huang, X. Fu, J. Li, Z. Yang, X. Liu, L. Pan and M. Xu, *Chemical Engineering Journal*, 2020, **392**, 123733.

34.   H. Zhu, Y. Wang, Y. Fan, J. Xu and C. Yang, *Advanced Theory and Simulations*, 2019, 1900016.

35.   B. Xiao, *Carbon Energy*, 2020, **2**, 251-264.

36.   S. Huang, L. Hou, T. Li, Y. Jiao and P. Wu, *Advanced materials*, 2022, **34**, e2110140.